Uncertainties in synthetic Meteosat SEVIRI infrared brightness temperatures in the presence of cirrus clouds and implications for evaluation of cloud microphysics

Fabian Senf[a], Hartwig Deneke[a]

[a]*Leibniz Institute for Tropospheric Research, Leipzig, Germany.*

Abstract

Synthetic brightness temperatures of five infrared Meteosat SEVIRI channels are investigated for their sensitivities on cirrus radiative properties. The operational SynSat scheme of the regional German weather prediction model COSMO-DE is contrasted to a revised scheme with a special emphasis on consistency between the model-internal ice-microphysics and infrared radiation in convective situations. In particular, the formulation of generalized effective diameters of ice, snow and graupel as well as subgrid-scale cloud cover has been improved. Based on the applied modifications, we first show that changed assumptions on the cirrus radiative properties can lead to 10 K warmer brightness temperatures. Second, we demonstrate that prescribed relative changes of 20% in cloud cover and particle size induce maximum changes of around 4 to 5 K. The maximum sensitivity appears for semi-transparent cirrus having brightness temperatures around 240 and 260 K and total frozen water path around 30 gm^{-2} for viewing geometries over Central Europe. We further consider the known COSMO-DE cold bias to discuss the problem of inconsistencies in model-internal and external formulations of cloud microphysical and radiative properties. We demonstrate that between 35% and 70% of the cold bias can be attributed to the radiative representation of cirrus clouds. We additionally discuss the use of window-channel brightness temperature differences for evaluation of model microphysics and hypothesize that the amount of COSMO-DE ice is overestimated in convective situations.

Keywords: Meteosat, Infrared brightness temperatures, Radiation, Ice-microphysics, Parameterization consistency

1. Introduction and motivation

Over the last decades, satellite observations have become indispensable data source for numerical weather prediction leading to substantial improvement in forecasting skill (Bauer et al., 2015). While the methods of using cloud-free hyperspectral infrared or microwave radiances from polar orbiting satellites together with variational data assimilation have reached a level of maturity in retrieving atmospheric profile information on global scales, the use of cloud-affected radiances of frequently observing, high resolution geostationary imagers remains one of the major challenges for data assimilation on the regional or convective scale (Bauer et al., 2011).

One major component of state-of-the-art data assimilation and model verification / evaluation strategies consists of the transfer of model data into observation space using computationally efficient radiative transfer models (e.g. Saunders et al., 1999), also called forward operators. Resulting synthetic satellite observations represent the simulated spatial distribution of the top-of-atmosphere outgoing radiation accounting for the spectral response of a chosen satellite sensor and can easily be compared to real observations. Synthetic satellite images derived for imaging radiometers have been used for model verification for more than twenty years. Morcrette (1991) used synthetic infrared Meteosat images to evaluate the diurnal cycles of surface temperature and cloudiness of the global ECMWF (European Centre for Medium-Range Weather Forecasts) model. He coined the term model-to-satellite approach. Roca et al. (1997) investigated the ability of a general circulation model to reproduce the observed relationship between tropical convection and subtropical moisture in the upper troposphere. The life-cycle of cloud systems and the diurnal cycle of cloud cover was further studied based on different model architectures with special emphasis on the representation of temporal and spatial variability in cloud forecasts (Chaboureau et al., 2000; Chevallier and Kelly, 2002; Slingo et al., 2004). For instance, Chaboureau et al. (2000) found an overestimation of the upper-level cloud cover in simulations of their Meso-NH model. Otkin et al. (2009) derived synthetic infrared MSG SEVIRI (Meteosat Second Generation Spinning Enhanced Visible and Infrared Imager) brightness temperatures for high resolution model runs and showed that the simulated brightness temperatures realistically depict many of the observed features. Using a joint analysis of window-channel brightness temperature distributions and cross-channel differences, they could identify limitations in their current cloud-microphysical scheme. Sensitivities of derived model forecasts and correspondingly of synthetic brightness temperatures to variations in microphysics and boundary layer parameterizations have been investigated by e.g. Otkin and Greenwald (2008) and Cintineo et al. (2014). Based on the comparison with observed cloud features as well as brightness temperatures, they identified the typical range of variations and the best performing schemes for certain cloud types. As model resolution steadily improves synthetic satellite images become increasingly important for the validation of deep convective processes (see e.g. Bikos et al., 2012).

For the German numerical weather prediction model COSMO-DE (Consortium for Small-scale Modeling - DE), a systematic bias in cold cloud cover was identified in several earlier studies (Pfeifer et al., 2010; Böhme et al., 2011; Eikenberg et al., 2015) which were using synthetic satellite images derived with the operational SynSat algorithm (Keil et al., 2006). It was found that the occurrence frequencies of brightness temperatures in the MSG SEVIRI 10.8 μm channel (BT10.8) at around 230 K are significantly overestimated by the model-based synthetic satellite images. Recently, Eikenberg et al. (2015) could show that the cold bias can be partially reduced when improvements to the microphysical parameterization, especially concerning the representation of ice nucleation processes as described in Köhler and Seifert (2015), are included.

For current data assimilation systems, the incorporation and beneficial use of cloud-affected satellite radiance is still challenging. For instance, Stengel et al. (2013) discussed the positive impact of the assimilation of cloud-affected infrared radiances on the moisture and geopotential height fields. Okamoto et al. (2013) assessed the use of the average cloud effect defined as difference between cloudy and clear-sky radiation for data assimilation purposes. Furthermore, Schomburg et al. (2014) established a concept for the assimilation of satellite-derived cloud properties within a mesoscale model using an ensemble Kalman Filter approach. All these data assimilation activities can benefit from a good assessment of uncertainties of synthetic satellite images in cloudy conditions.

However, one current problematic aspect in the simulation of synthetic satellite images is that often differing and contradicting assumptions on the properties of hydrometeors are applied in the model microphysics and in the radiative transfer. Therefore, several variables that are derived from the prognostic model variables via diagnostic schemes, for instance subgrid-scale cloud cover and effective particle size, are to some degree unconstrained. This can introduce uncertainties in the synthetic radiances and partially complicates the interpretation of observed model biases and their sensitivity to model changes. To address that issue, a more strict reformulation of subgrid-scale parameterizations imposing self-consistency has been proposed (Baran, 2012; Baran et al., 2014a,b; van Diedenhoven et al., 2014) in which essentially the same assumptions about hydrometeor properties are applied to the model-internal microphysical and radiative calculations. For instance, Baran et al. (2014b) established a parameterization of microphysical ice crystal properties that preserves the physical consistency between the cloud physics and radiation schemes across a large range of wavelengths in climate model simulations. They pointed to the importance of the choice of the particle size distributions as well as the assumed shape mixtures. Moreover, we like to emphasize that self-consistency should also be extended to model-external calculations that deal with the simulation of synthetic observations using forward operators and with the derivation of cloud properties using observation-based retrieval algorithms. Within that line, Thompson et al. (2016) provided a recent study in which effective radii of cloud water, cloud ice, and snow were diagnosed based on assumptions in the model microphysics scheme. The authors could show that the subsequent use of consistently derived effective particle sizes in the model-internal radiation calculations and in the satellite forward operator can improve the agreement with observations.

Furthermore, the ice-microphysics parameterization faces the challenge that a distinction of frozen condensate in categories, e.g. ice, snow and graupel, with predefined characteristics is inherently artificial and often done without a strong theoretical or empirical basis (see e.g. Morrison and

Milbrandt, 2015, and discussion and references therein). Due to their importance on the global scale, shortcoming in the representation of cirrus-microphysical and radiative properties can lead to significant errors in weather forecasts and climate predictions (see e.g. Waliser et al., 2009). In addition, Waliser et al. (2009) discussed that difficulties in the interpretation of simulated frozen hydrometeor variables can delay progress in model improvements, especially when suspended cloud ice is distinguished from precipitating particles and when observations or retrievals are highly sensitive to different parts of the hydrometeor size spectrum. This emphasizes the central point of our paper that a consistent description of hydrometeor radiative properties is needed across the full range of the electromagnetic spectrum, also in view of the synergistic utilization of future multi-sensor active and passive satellite observation (see e.g. Illingworth et al., 2015).

The primary goal of our study is to quantify and understand uncertainties in synthetic brightness temperature which arise from various assumptions about microphysical properties of frozen hydrometeors and subgrid-scale cloud cover in realistic cloud scenes. We therefore introduce the Meteosat and COSMO-DE data in Sect. 2. The simulation of cloud-affected radiances via the operational scheme as well as with the revised scheme is explained in Sect. 3. Systematic changes and sensitivities to perturbations of cloud properties are assessed in the results section 4. A discussion on the origin of emerging uncertainties and implication for the interpretation of model biases is examined in Sect. 5. Finally, conclusions are given in Sect. 6.

2. Data

2.1. Infrared MSG SEVIRI data

This study uses observational data and sensor characteristics of five infrared channels of the imaging radiometer Spinning Enhanced Visible and Infrared Imager (SEVIRI) aboard the geostationary Meteosat Second Generation (MSG) satellites operated by EUMETSAT (Schmetz et al., 2002). The studied channels are centered around 6.2, 7.3, 8.7, 10.8 and 12.0 μm and form a subset of all available SEVIRI channels comprising all together of 11 narrow-band and one broad-band high-resolution visible channel. We focus on data of the primary scan service, which has an orbital position at zero degree longitude and an image update cycle of 15 minutes. We concentrate on the domain covered by the forecast model COSMO-DE, which is further described in the next section. The SEVIRI narrow-band channels have approximately a resolution of 4×6 km^2 in this domain which is coarser than the COSMO-DE grid size of 2.8×2.8 km^2 (see next subsection). Before comparison with synthetic satellite images, SEVIRI observations are regridded onto COSMO-DE grid using nearest-neighbor interpolation.

The selected SEVIRI channels essentially fall into two categories: water vapor and window channels. In the 6.2 and 7.2 μm channels, water vapor absorption and emission is strongly influencing the outgoing radiation. The transmissivity of a cloud-free atmosphere is lower in the 6.2 μm channel leading to an increased effective emission altitude compared to the 7.3 μm channel. This altitude is around 9 and 7 km for the 6.2 and 7.3 μm channels, respectively, with a typical variation of 1 km in both channels due to variations in atmospheric temperature and moisture. Clouds affect the outgoing thermal radiation at 6.2 and 7.3 μm, if the cloud-top height is close to or higher than the effective emission altitude. The other three channels, centered around 8.7, 10.8 and 12.0 μm, fall into the window channel category. They are less affected by atmospheric gases and show the radiative signature of surface, clouds, aerosols or a combination of these. As the liquid and ice cloud emissivities are slightly different for all the three window channels, cross-channel brightness temperature differences (BTDs) carry information about in-cloud microphysical properties such as cloud phase and ice crystal size (see e.g. Strabala et al., 1994; Pavolonis, 2010). This is further illustrated by Table 1. Typical penetration depths - calculated after Petty (2006) as the inverse of the apparent extinction coefficient $\tilde{\beta}^{-1}$ (see Sect. 3.1 for more discussion on radiative properties) - for various homogeneous cirrus clouds with a constant generalized effective diameter are listed there. Penetration depth is strongly decreasing with increasing cloud-optical depth which is for the considered cases linked to the particle size. The difference in real and imaginary part of ice refractive index determines the difference in absorption and scattering properties at 8.7, 10.8 and 12.0 μm wavelength. Relative to the behavior at 10.8 μm, the penetration depth at 8.7 μm (12.0 μm) is around 17 % larger (smaller) for low ice water content (IWC), leading to positive BTDs for the two channel combinations. This difference shrinks or even changes sign for increasing IWC. The difference in penetration depths is mainly caused by the difference in absorption cross sections per ice crystal which are also listed in Tab. 1. Absorption cross section increases about 20% going from 8.7 to 10.8 and further to 12.0 μm for smaller particles. In contrast, scattering cross sections for small ice particles have lower values at 10.8 μm whereas scattering is most pronounced at 8.7 μm. The absorption and scattering behavior for the considered wavelengths significantly changes for liquid cloud droplets. Furthermore, the difference between BTs at 10.8 and 12.0 μm for cloud-free situations can be related to the near-surface moisture content and is typically negative (see e.g. Chesters et al., 1983).

2.2. Convection forecasts from COSMO-DE

COSMO-DE is the operational short range weather forecast model of the German weather service (Baldauf et al., 2011). It is a convection-permitting non-hydrostatic numerical weather prediction model with a horizontal grid spacing of 2.8 km initialized each 3 hours running 21 hours ahead. The model domain covers Germany, Switzerland, Austria, and parts of neighboring European countries.

We utilize forecasts for 74 days in the years 2012 (25 days), 2013 (25 days) and 2014 (24 days) with deep moist convection present in the domain of COSMO-DE. The convection days have been chosen as basis for our study mainly for two reasons. First, the cloud scenes are highly complex in convective situations, which makes consistent radiative transfer calculations (even in the infrared) quite challenging. Deep convective clouds, precipitating and non-precipitating cirrus clouds as well as several other cloud types coexist comprising a size and shape mixture of a multitude of different hydrometeors. Second, the performance of the forecast model as well as the rapid use of observational data is of special importance in convective situations. For the subjective case selection, MSG SEVIRI observations, severe weather reports found in media and news as well as ECMWF forecasts of convective instability and other related instability indices have been used. For four initialization times (3, 6, 9, 12 UTC), the six-hours ahead model forecasts were chosen and retrieved from the data archive, corresponding to the image time slots of 9, 12, 15 and 18 UTC. All together, this results in 296 scenes (more than 57 million profiles) for which synthetic satellite images have been calculated and which were taken as basis for the determination of image uncertainties.

One arbitrary example scene (5 July 2012 at 12 UTC / 13 LT) is shown in Fig. 1. Convective clouds are starting to develop in the southeastern part of the model domain identifiable by the spherically shaped, cold cores. Remaining cirrus cloud cover is also visible in several parts of the domain. The forecast ice water path (IWP) and snow water path (SWP), additionally shown in Fig. 1b-c, share nearly the same spatial distribution. The high values of graupel water path (GWP) (in Fig. 1d) mainly confined to the convective cores. Graupel significantly less wide-spread than ice or snow. Around 74% of the domain is covered with clouds containing ice, 84% is covered with precipitating snow, but only 26 % with graupel. The median IWP and SWP over all cloudy parts is around 8 gm^{-2} for both categories. The total frozen water path (FWP) reaches domain-median values around 16 gm^{-2}. More than 78% (69%) of the ice(snow)-containing cloud columns have a content less than 30 gm^{-2} or equivalently cloud-ice (snow) emissivities smaller than around 0.87 (0.5) which illustrates that semi-transparency is a common situation in these convective scenes. Due to the wide range of cloud-optical thicknesses, a broad range of BT10.8s can be found for semi-transparent cirrus clouds, with cold BTs up to 220 K for thicker cirrus and BTs close to surface temperatures for very thin clouds. Furthermore it becomes apparent, that all frozen hydrometeor categories (but mainly ice and snow) contribute to outgoing infrared radiation and should be taken into account, accordingly. Fig. 1 also shows the Meteosat observation of BT10.8 and retrieved FWP for illustration. By comparison with the simulation, it is apparent that spatial distribution of convectively developing clouds, their vertical extent and the stage in their convective life cycle is not perfectly represented by the model simulation. Furthermore, the residual cirrus cloud cover seems to be overestimated by the model. However, the simulated FWP-values appear in a plausible range considering the limited observational sensitivity for lower as well as larger FWP-values (see e.g. Waliser et al., 2009, and references therein for some discussion on typical limitations of IWP retrievals).

2.3. COSMO-DE ice microphysics

For the parameterization of cloud microphysical processes, COSMO-DE operationally applies a one-moment scheme that predicts prognostically five hydrometeor classes by their mass fraction: cloud water, cloud ice, precipitating snow, rainwater and graupel (Baldauf et al., 2011). Cloud ice consists of small ice crystals suspended in air with no relevant motion relative to the flow of moist air. The distribution of cloud ice is assumed to be monodisperse. COSMO-DE ice crystals are assumed to consist of small hexagonal plates. COSMO-DE snow is assumed to be exponentially distributed and made of aggregates or a dendrite-like habit. COSMO-DE graupel is also assumed to be exponentially distributed with lump graupel-like habit. Conversion processes between ice or snow and other hydrometeor classes and/or water vapor involve a multitude of processes, for instance heterogeneous nucleation of cloud ice, deposition growth and sublimation, riming and autoconversion due to aggregation as well as melting and freezing. On the one hand, it seems to be obvious that the complexity of conversion processes demands simple enough assumptions on the size distributions and shapes or shape mixtures of the concerned hydrometeors. On the other hand, an accurate evaluation of microphysical processes is only possible if the same assumptions on hydrometeor properties are consistently applied within the simulation of synthetic observations which are later used for evaluation.

In general, a subgrid-scale cloud cover parameterization estimates the fraction of cloud-covered area within a grid box, which is also connected to the fraction of cloudy air volume to the total grid box volume and henceforth to the in-cloud hydrometeor mass contents. Subgrid-scale cloud cover results from combined fluctuations of temperature and moisture / condensed water content due to turbulent or organized motion with spatial scales smaller than a model grid box (Sommeria and Deardorff, 1977). The fluctuations lead on the one side to partially sub-saturated air volumes in on average cloudy grid boxes, and on the other side to partially super-saturated air volumes in on average cloud-free grid boxes. COSMO-DE is applying a subgrid-scale cloud cover parameterization based on relative humidity and similar to the scheme of Sundqvist et al. (1989), which involves a comparison of the total water relative humidity against a so-called critical humidity threshold (see e.g. Quaas, 2012, for further discussion on critical humidity). In addition to the standard formulation, the COSMO-DE cloud cover is empirical corrected for ice clouds using a correction factor that is monotonically decreasing for decreasing specific frozen water content. The correction factor has been adjusted over time, and we are aware that systematic changes also have been made during our time period of interest (Görsdorf et al., 2011).

3. Methods

3.1. Cloudy radiances with RTTOV

The radiative transfer model RTTOV (Saunders et al., 1999) is operationally used by several national weather services to simulate synthetic satellite images for numerical model forecasts (e.g. Slingo et al., 2004; Keil et al., 2006). The simulation of RTTOV ice-affected radiances is structured in several steps. In the first step, the macroscopic model variables representing the ice water content (IWC) and temperature (T) within one grid box are converted into microphysical properties of the cirrus clouds represented by a generalized effective diameter (D_{ge}). In the next steps, ice-radiative properties are calculated from D_{ge} using relations presented by Fu (1996). An apparent extinction coefficient $\tilde{\beta} = \beta_{abs} + b\,\beta_{sca}$ is calculated after Chou et al. (1999), where β_{abs}, b and β_{sca} denote absorption coefficient, backscattering function, and scattering coefficient, respectively. Finally, $\tilde{\beta}$ is provided to the radiative transfer code which simulates the cloud-affected radiances.

In the standard RTTOV code, the user can choose between four different empirical relations for the IWC-to-D_{ge} conversion. They have been derived from in-situ measurements of cirrus clouds in the past by several authors. For the calculation of radiative properties, the user can select one of two different ice crystal shapes, randomly-oriented hexagonal columns and aggregates. Please note, that these two intermediate steps involve assumptions about the distributions, orientations and shapes of ice crystals that are typically diagnosed differently from the model microphysics.

3.2. Operational SynSat

The operational SynSat is a diagnostic tool that builds up an interface to RTTOV (version 9.3 for 2012, and version 10 later) implemented by Keil et al. (2006). It prepares COSMO-DE profiles of thermodynamic and hydrometeor variables as well as surface fields and simulates synthetic cloud-free and cloud-affected radiances of 8 infrared channels of MSG SEVIRI. Three major limitations for the derivation of ice-affected radiances are discussed below, further details about the current operational SynSat setup have been carefully collected by Eikenberg et al. (2015).

The operational SynSat has one main limitation that it can only handle one frozen hydrometeor category for which microphysical and radiative properties are calculated. This leads to the question of how to combine cloud ice, precipitating snow and graupel for more consistent radiative transfer calculations and of how much radiative impact can be attributed to each simulated hydrometeor species. It has been recently argued by Kostka et al. (2014) that for the mixed frozen hydrometeor content, snow should only partially included to account for the reduced optical thickness of larger snow crystals. For instance, the authors suggested to account for only 10% of the snow mass in their visible-range radiative transfer calculations.

The second limitation of the operational SynSat concerns the relationship between hydrometeor mass content, effective particle size and shape, and radiative properties. The operational SynSat scheme uses the coefficients of the base case of McFarquhar et al. (2003) (see their table 2) to convert the ice water content (IWC) that is actually the sum of cloud ice, snow and graupel mass content, into a typical crystal size, namely the generalized effective diameter D_{ge}. The McFarquhar bulk parameterization only incorporates the frozen hydrometeor mass content as predictor (i.e. no explicit temperature dependence) and was derived from in-situ measurements of size and shape in tropical anvil clouds (see Fig. 2). Furthermore, the mixture of frozen condensate is assumed to have hexagonal shape for the calculation of radiative properties. The two assumptions about the particle size and shape are, however, partially inconsistent with the model-internal microphysical formulations.

As a last point, we like to address the subgrid-scale cloud cover parameterization (f). The operational SynSat formulation already uses f from the model-internal broadband radiation scheme. It does however introduce an artificial threshold based on the snow mass fraction q_s, in which cloud cover is set to one for $q_s > 10^{-7}$ kg kg^{-1}. This procedure strongly enhances the longwave radiative effect of precipitating snow and all other hydrometeors within the affected grid box.

3.3. Revised SynSat scheme

For our study, we use RTTOV version 11.2 to simulate synthetic images with the sensor characteristics of MSG SEVIRI. We propose a revised SynSat scheme, and therefore perform two basic modifications in the SynSat interface. Both aim to increase consistency with model-internal formulations of considered processes. The first adjusts the subgrid-scale cloud cover in the satellite forward operator to fully match the formulation in the model radiation scheme, and the second is concerned with the derivation of an effective crystal size based on model microphysics.

First concerning subgrid-scale cloud cover, the operational scheme introduces an artificial threshold and henceforth an increased radiative impact of precipitating snow. However, it seems to be physically plausible that also the snow category exhibits a subgrid-scale structure where the grid box area occupied by snow is also determined by the same subgrid-scale cloud-cover value. We therefore propose to use the basic cloud cover variable without any threshold to ensure consistency with the model-internal broadband radiation scheme.

Second, we propose to replace the operationally-used IWC-to-D_{ge} conversion scheme with one more consistent with the COSMO-DE microphysics. Therefore, the generalized effective diameters of the frozen hydrometeor categories ice ($D_{ge,i}$), snow ($D_{ge.s}$) and graupel ($D_{ge.g}$) have been directly diagnosed from the model assumptions. Details on this calculation are given in Appendix A. A comparison of occurrence frequencies of the generalized effective diameters of ice $D_{ge,i}$, snow $D_{ge,s}$ and graupel ($D_{ge.g}$) to D_{ge} calculated from the McFarquhar base case is shown in Fig. 3 for all categories, separately. The histograms are constructed from all selected 296 COSMO-DE scenes. The spread in ice and snow occurrence frequencies is due to the assumed dependence of the respective particle size distribution on temperature (see Appendix A). COSMO-DE ice is appearing in a much broader range of particle sizes with significant occurrence frequencies between 0 and 80 μm. The highest frequencies in ice particle size occur at the right edge of the populated histogram area at which COSMO-DE ice exists at cold temperatures around 210 K and has smaller particle sizes than predicted by the McFarqhuar scheme. The accumulation of extremely small crystal sizes might be physically unrealistic and can be a consequence of an overestimated sensitivity of particle size to temperature. As consequence, these unrealistically small ice crystals will lead to artificially low brightness temperatures for these clouds by increasing the ice-cloud optical depth. The distribution of COSMO-DE snow is generally shifted towards larger particle sizes. For instance, a McFarquhar-based $D_{ge,s}$ of 20 μm corresponds to a COSMO-DE snow diameter between 70 to 80 μm giving a factor of up to four in increase of diagnosed particle size. The COSMO-DE graupel size does not depend on temperature, therefore $D_{ge,g}$ and the McFarqhuar-D_{ge} fall onto one line. The estimated graupel particle size is significantly larger than D_{ge} based on the McFarqhuar scheme. The relative occurrence frequencies of COSMO-DE ice, snow and graupel particle sizes are shown in Fig. 3d. The maximum frequencies appear at 15, 80 and 50 μm diameter of ice, snow and graupel, respectively. There is significant overlap between sizes of the different categories, especially in the range between 50 and 100 μm. Figs. 3e-f show the distributions of the water path of all the individual categories, as well as their relative contribution to the total frozen water path. IWP and SWP peak around 10 gm^{-2}, GWP has a broad maximum close to 1 gm^{-2}. The IWP distribution is more narrow than the SWP distribution and approaches zero at around 100 gm^{-2}. SWP and total frozen water path FWP are very similarly distributed. Snow is dominating FWP for small and large FWP-values. Between 1 and 100 gm^{-2}, IWP reaches comparable magnitudes. The contribution of graupel to the total frozen water path is negligible.

The radiative properties of ice $\beta_{abs,i}$, $\beta_{sca,i}$ and b_i and snow $\beta_{abs,s}$, $\beta_{sca,s}$ and b_s have been calculated using the internal RTTOV fit relations and parameters. COSMO-DE ice is considered as hexagonally shaped and COSMO-DE snow as aggregates. Please note, that this step is the weakest point in our revised scheme as it still relies on RTTOV empirical relations which presume a certain shape and particle size distribution for the considered hydrometeors. For extrapolation of optical properties, the geometric optics limit was applied for $D_{ge} > 118$ μm. For small $D_{ge} < 12$ μm, D_{ge} was simply set to 12 μm. The absorption and scattering coefficients of COSMO-DE graupel have been separately calculated based on so-called Mie theory (Goody and Yung, 1989, p.315ff.) assuming that spherical shape is a sufficient assumption for graupel particles. Please note that all later results are essentially unaffected by a potential exclusion of graupel from infrared radiative transfer. The radiative properties of the different categories, including the liquid, have been added using standard mixing rules (see e.g. Baum et al., 2011, Eqns. (B1), (B2) and (B8)). This strategy solves the problem of mixing different frozen hydrometeor categories on a basic level which is however only possible since RTTOV version 11. This version supplies a newly implemented interface (RTTOV method 2) which allows for user-defined radiative properties. We also developed an approximate method for category mixing using older RTTOV versions which is explained in Appendix B.

Subgrid-scale liquid cloud hydrometeor contributions have been ignored for simplicity which will affect the warmer portion of the BT10.8 spectrum. Radiative contributions of rain have also been neglected which have a relatively small impact on the simulated infrared brightness temperatures, but will be more important for longer wavelengths, e.g. in the microwave range. In addition, infrared surface emissivities from the monthly-mean University of Wisconsin Global Infrared Land Surface Emissivity Database (UWIREMIS) have been used within RTTOV for an improved representation of surface characteristics (see Vogel et al., 2011, and references therein).

3.4. Sensitivity setups

The revised scheme is investigated for its sensitivities to perturbations in subgrid-scale cloud cover f and crystal size D_{ge}. Both parameters can show large natural variability depending sensitively on the local thermodynamic state and on the pathway of realized cloud processes.

In the following, we define perturbations of cloud cover δf and effective particle size δD_{ge} based on physically plausible relative changes, which are subsequently used to quantify the sensitivity of simulated BTs to the parameterization of both quantities. Radiative transfer calculations are independently carried out with different perturbed parameter sets and compared to a reference calculation without perturbation. For instance, BT10.8 fields $T_{10.8}^{(+\delta f)}$ and $T_{10.8}^{(-\delta f)}$ are obtained for perturbations in cloud cover $f + \delta f$ and

$f - \delta f$, respectively, and the resulting sensitivity is defined as

$$\Delta T_{10.8}^{\delta f} = \sqrt{\frac{1}{2}\left(\left(T_{10.8}^{(+\delta f)} - T_{10.8}^{(*)}\right)^2 + \left(T_{10.8}^{(-\delta f)} - T_{10.8}^{(*)}\right)^2\right)} \tag{1}$$

where $T_{10.8}^{(*)}$ denotes the BT10.8 of the reference simulation. A similar definition is applied to obtain the sensitivity to D_{ge}-perturbations. Uncertainty in the clear-sky part of the infrared radiation is not considered. Multi-scattering effects due to infrared horizontal photon transport have also been neglected in our current approach, even though they might become important for the estimation of longwave heating rates on scales of one kilometre or less (see Klinger and Mayer, 2016, for recent parameterization development). δf and δD_{ge} are estimated as follows.

We first use the observed uncertainties in the so-called critical relative humidity threshold to estimate a typical magnitude of cloud cover perturbations δf. Quaas (2012) discussed that subgrid-scale cloud cover f is usually parameterized by comparing the grid box-averaged total water relative humidity to a critical relative humidity profile r_c, which is meaningfully chosen or empirically determined. A similar approach has been applied in COSMO-DE (see Sect. 2.3). Quaas (2012) compared several observation-based estimates and model implementations, and showed that a significant spread exists between all of them. Based on his Fig. 4, we infer that typical r_c values are around 0.4 in the middle to upper troposphere, with a variation δr_c of 0.1 at spatial scales of several hundred kilometers. Quaas (2012) further discussed the mathematical link between f and r_c. Assuming a simple uniform subgrid-scale probability distribution of total water specific humidity, the variations in cloud cover are given by (based on eq. (1) of Quaas

(2012))

$$\frac{\delta f}{1-f} = -\frac{1}{2}\,\frac{\delta r_c}{1-r_c}\,. \tag{2}$$

The pre-factor 1/2 depends on the assumed shape of the probability density distribution and increases, for instance, to 2/3 if a triangular shape is considered (see eq. (4) of Quaas (2012)). By applying the r_c-calculation to the COSMO-DE fields, median values of r_c between 0.85 and 0.9 have been found due to the much higher spatial resolution and the larger amount of resolved water vapor variability. Assuming that $\delta r_c \approx 0.05$ at these scales, a resulting $(1-f)$-perturbation between 15 and 25% is estimated from eq. (2). For our sensitivity setup, δf is henceforth set to $0.2(1-f)$, i.e. 20% relative perturbation of clear-sky fraction. f-values beyond the range of 0 and 1 are set back to the interval bounds.

For the second sensitivity setup, we estimate the magnitude of typical crystal size perturbations. We refer back to Fig. 2 as visualization of the IWC-D_{ge} relation analyzed by McFarquhar et al. (2003). For instance, an ice water content of 0.5 gm^{-3} leads to a generalized effective diameter of 100 μm with a local penetration depth of around 200 m and an infrared apparent optical thickness of 5.7 assuming a 1-km thick cirrus cloud (see Tab. 1). The $\pm\sigma$ and $\pm 2\sigma$ intervals in Fig. 2 can be seen as representative for the uncertainty in fitted parameters, and visualize the typical spread in observational microphysical data. As indicated by error bars, the typical spread for the considered mass content is around 20 μm, i.e. 20 % relative deviations due to intrinsic uncertainties in the bulk parameterization. Based thereon, we apply $\delta D_{ge} = 0.2 D_{ge}$ within two perturbed simulations for sensitivity study. For simplification, effective particle size of all frozen condensate categories, ice, snow and graupel, are collectively shifted at once by an amount of δD_{ge} depending on the local condensate size. The $D_{ge} \pm \delta D_{ge}$ is inserted in the calculation of radiative hydrometeor properties, however, keeping the average particle mass fixed (see appendix Appendix C for more details).

4. Uncertainties in synthetic brightness temperatures

4.1. Impact of systematic changes

The consequences of the revised cloud cover formulation can be seen in Fig. 4(a) and 4(d) for the same example as in Fig. 1. The change in BT10.8 is mainly positive throughout the domain, and values easily exceed 10 K for semi-transparent cirrus clouds. The occurrence frequency bias of BT10.8 with revised cloud cover relative to the operational setting is shown in Fig. 5(a). For the scene in Fig. 4, we see that the warmer BTs due to cloud-cover changes mainly affect the relative occurrence frequencies around 220 K and 280 K, where a maximum reduction of 60% is found for the former and an increase of around 50% for the latter. For all considered cases, the maximum relative reduction appears in a broader range between 220 and 240 K with scene-to-scene median values between 5 to 20%. The scene-to-scene inter-quartile range shows that more than 50% reduction of values around 220 K is obtained for at least one quarter of the case set. The reduction of cold BTs is partially compensated by an increase of warmer BTs between 280 and 300 K. For the frequency bias relative to the observed BT10.8 distribution (shown in Fig. 5(d)), we recognize that the cloud-cover change leads to a significant reduction of the cold bias around 230 K which is discussed in more detail in Sect. 5.

In addition, the effect of the revised crystal size formulation can be seen in Fig. 4(b) and 4(e) for the operational, and in Fig. 4(c) and 4(f) for the full revision of the SynSat algorithm, respectively. The picture of BT10.8 changes is more indifferent and changes can be positive as well as negative. The highest sensitivity for changes in BT10.8 appears to be in a small BT range around 220 K. A median reduction of the BT10.8 frequencies around 220 K up to 40% relative to the operational setting occurs for the revised particle size diagnostics (see Fig. 5(b)) which might be a result of the pronounced increase in snow effective diameters. This reduction also acts to reduce the cold bias relative to the observation around 230 K (see Fig. 5(e)), however less strongly than the cold-cover change. Finally, the combination of revised cloud cover and particle size diagnostics gives an overall reduction of cold BT occurrence frequencies of up to 50% relative to the operational setting and an compensating increase in warmer BTs of around 10%.

4.2. Sensitivities due to cloud cover perturbations

Relative perturbations of 20% of the subgrid-scale cloud free part have been applied to the simulation the synthetic radiances using our revised scheme. Fig. 6a shows the resulting standard deviation of the BT10.8 defined by eq. (1) for the example scene introduced in Fig. 1. The BT variations can be as large as 4 K and mainly appear for semi-transparent clouds. The systematic changes by introducing modifications in cloud cover and crystal size by our revised scheme can, however, introduce significantly larger changes in BT10.8 for the given example scene.

The occurrence frequencies of BT deviations due to cloud cover perturbations conditioned on the average BTs are shown in Fig. 7a-c for 3 MSG SEVIRI channels at 6.2, 7.3 and 10.8 μm and in Fig. 7d-e for the window-channel differences between 10.8 and 12.0 μm as well as 8.7 and 10.8 μm for all 296 COSMO-DE scenes. The sensitivity is largest for intermediate

BTs. The conditioned 25-th, 50-th and 75-th percentiles of the occurrence of BT deviations are also plotted in Fig. 7. With less than 0.5 K, the median curves show smaller maximum values for the water vapor channels than for the infrared window channels. Therefore, the sensitivities are in the same order of or less than the RTTOV accuracy itself (Matricardi et al., 2004) for these channels and might play a minor role. In addition, occurrence frequencies of the BT deviation conditioned on intervals of total frozen water path are given in Fig. 8. For cloud cover perturbations, the maximum BT uncertainties occur around 10 gm^{-3} for viewing zenith angles typical for Central Europe and decrease back to zero for smaller as well as larger FWP values. The individual perturbations of the 3 window-channel BTs share very similar distributions (not shown), because fractional subgrid-scale cloud cover reduces the effective cloud emissivity by an equal fraction for the different wave lengths. The resulting compensation leads to relatively small BTD deviations.

4.3. Sensitivities due to crystal size perturbations

The effective crystal sizes of ice $D_{ge,i}$ and snow $D_{ge,s}$ have been collectively varied by ± 20 % before radiative properties and henceforth synthetic infrared brightness temperatures have been simulated. The resulting BT10.8 deviations (see Fig. 6b) reach maximum values between 4 and 5 K in semi-transparent cirrus clouds and leading to ring like structures around convective cores. There are mainly two effects that contribute to BT variations. First, for thinner semi-transparent cloud layers, the temperature is approximately constant across the layer, hence the whole cloud emits with a nearly constant blackbody temperature. The outgoing radiation is a mixture of the thermal radiation of the cloud itself and the partially attenuated incident radiation from below. It is termed here as the clear-sky contribution for simplification. Changes in the ice particle size lead to changes in the cloud optical thickness and transmissivity, thus modifying the weighting between the cloudy and clear-sky part. The amplitude of BT variations is proportional to the contrast between the cloudy and clear-sky radiances, which is a measure of thermal radiation loss by ice clouds. It is generally larger for atmospheric window channels compared to the water vapor channels.

The second effect is connected to the temperature gradient within the cloud layer, and is much less important than the first effect mentioned above. For opaque clouds, the upwelling radiation above the cloud is a mixture of the radiation coming from the top layers. The measured brightness temperature seems to originate from an emission layer located approximately one penetration depth below the cloud top (see Tab. 1). Perturbations in the particle size thus lead to variations in penetration depth and in the emitted radiance.

The occurrence frequencies of BT deviations due to ice crystal perturbations conditioned on the occurrence of an average BT are also depicted in Fig. 7 for 3 MSG SEVIRI channels and two window-channel differences. For coldest and warmest average BTs, the uncertainty approaches small values. The coldest BTs are found in convective cores, which are optically thick and thus insensitive to perturbations in the particle size. In contrast, the warmest BTs are not or only very weakly affected by the thermal radiation of highly transparent cirrus clouds. In this situation with high surface or low cloud emission, perturbations in the ice radiative properties changes the BTs only marginally. The median BT deviations due to crystal size perturbations are typically a factor two to three larger than the ones due to cloud cover perturbations. The given distributions are slightly skewed to warmer average BTs. For BTDs shown in Fig. 7i-j, the uncertainty increases towards more positive BTDs which occur for smaller particle sizes and/or lower cirrus optical thickness (see discussion at Sect. 2.1). Largest deviations of BTD are around 1 K. The occurrence frequencies of deviations of BT conditioned on total frozen water path (see Fig. 8b) show the maximum BT sensitivity shifted to values around 30 gm^{-3} for Central European viewing geometry. The highest sensitivity of BTDs occurs close to 10 gm^{-3} with median deviations around 0.5 K, this means the BTDs are more sensitive to thinner cirrus cloud than the BTs itself. For large FWPs, cloud optical thickness is larger and clouds are essentially opaque. The apparent BT deviations are then mainly determined by variations in the penetration depth as discussed above.

5. Implications for evaluation of cloud microphysics

5.1. From model inconsistencies to uncertainties

The lack of knowledge and consistency in the different descriptions, and thus different stages of approximation, of hydrometeor properties in different parts of the numerical model causes uncertainties in derived synthetic observations. We have chosen COSMO-DE forecasts as an example, but the problem of intrinsic model inconsistencies of interacting subgrid-scale processes is a general issue for numerical forecast models. Model inconsistencies can cause fundamental conflicts which cannot be easily reconciled.

In recent years, growing interest has been directed towards this problem of inconsistencies. For instance, Baran (2012) stated that a "fundamental problem with the traditional approach is that it does not directly couple cloud physics and radiative parameterizations. This situation is physically unsatisfying." More recently van Diedenhoven et al. (2014) argued that "Selfconsistency within a model dictates that the same ice volume, area, and aspect ratio used in an ice microphysics scheme should also be used in a model's radiative transfer scheme". We want to extent the list. It is also important to employ similar formulations of microphysical and radiative properties between the forecast model and the so-called forward operators. These simulate synthetic observations, which can be used to constrain the model via data assimilation or to evaluate the model performance in observation space.

To address the problem of intrinsic model inconsistencies in the future, we emphasize that special attention should be paid to variables which induce significant sensitivities in synthetic observations, for instance crystal size, shape and orientation. In the reformulation of the subgrid-scale processes these variables should be consistently incorporated in all relevant processes in a way that the model state vector and temporal evolution, i.e. the prognostic tendencies, fully depend on them (see e.g. Baran et al., 2014a,b, for recent development). This procedure strongly constrains these variables and reduces associated ambiguities, a progress that would be highly beneficial for applications like data assimilation or forecast verification even if the actual model skill might be partially degraded at first.

5.2. Interpretation of model biases

A specific application of our sensitivity analysis of ice-affected BTs is discussed next. COSMO-DE has a known deficit concerning cold cloud cover termed cold bias (Pfeifer et al., 2010; Böhme et al., 2011). The cold bias shows up as an overestimation of occurrence frequencies of synthetic 10.8 μm BTs in the range between 240 and 220 K, as well as an underestimation of the former in the range between 250 and 290 K. It has been discussed by Eikenberg et al. (2015) that the cold bias is related to possible deficits in the parameterization of heterogeneous ice nucleation and cloud ice sedimentation.

For our set of convective scenes, the median occurrence frequencies of BT10.8 are shown in Fig. 9 for the observation, the operationally generated synthetic BTs, and for the BTs from our revised setup. The histogram based on the observation has a maximum between 280 and 290 K and then decreases to colder BTs relatively monotonically. All synthetic BT histograms show a slight shift of the major maximum to warmer BTs, and a pronounced secondary peak around 225 K. In terms of deviations relative to the observed frequencies, the median overestimation of the secondary peak is around $167 \pm 20\%$ for the operational synthetic BTs, where the interval gives an uncertainty estimate of the average due to the scene-to-scene variability. The underestimation of operationally-determined BT occurrence frequencies is maximal around 265 K with a relative magnitude of $-35 \pm 3\%$. For the recalculated synthetic BTs, the secondary peak slightly shifts from 226 to 229 K and the median overestimation of the secondary peak magnitude decreases to $63 \pm 13\%$ relative to the observed frequencies. When the differences between the absolute frequencies between the operational SynSat secondary peak and the observation are compared to the reduced peak magnitude from the revised scheme, we identify that the absolute difference reduces by around 50 %.

In general, the secondary peak magnitude is sensitive to systematic model-internal changes in the subgrid-scale cloud cover. For instance, a switch in parameters that determine COSMO-DE subgrid-scale cloud cover took place after the summer season in 2012. Afterwards, higher f-values were predicted for similar saturation conditions. This change in model-internal cloud-cover parameterization should have significant influence on the simulated satellite imagery which is the case for our revised scheme. The operational SynSat implementation, however, does not show this sensitivity due to an insufficient coupling between model-internal and satellite forward operator assumptions. Based on our revised BT calculations, we can identify that the change in cloud cover lead to a significant degradation of model skill in terms of simulated cold BTs. A smaller overestimation of the peak of $18 \pm 15\%$ in 2012 drastically increased to $126 \pm 20\%$ for the years 2013 and 2014. Such a significant change is not observable in the operational BTs. Fig. 9 also shows the range between median occurrence frequencies of the $\pm 20\%$ particle size perturbations. The impact is generally small and largest in the BT-range of the secondary peak. The overestimation relative to the observation is 41% and 102% for particle size perturbations of 20% and -20%, respectively. When the absolute deviation between the simulated frequencies at the secondary peak are compared to the observation, we find that the absolute overestimation reduces to 35% and 70% for particle size perturbations of 20% and -20%.This leads us to the conclusion that 30% to 65% of the cold bias can be attributed to the radiative representation of cirrus clouds for the considered set of forecasts.

In addition, Fig. 9 shows the occurrence frequencies of the cross-channel BTDs between 10.8 and 12.0 μm as well as 8.7 and 10.8 μm. Both infrared channel differences carry information about the hydrometeor phase, shape and size (see e.g. Sect. 2.1 as well as Yang et al., 2015, and references therein). The observed $(T_{10.8} - T_{12.0})$-frequencies range from -1 to 7 K, with a single broad peak between 1 and 2 K induced by radiative contributions of clear-sky and cloudy radiances (see also Fig. 10). The observed scene-to-scene variability is large for intermediate values. The simulated ($T_{10.8} - T_{12.0}$)-frequencies show a steeper increase at the left tail of the distribution, a less steep decay at the right tail and an underestimation of the occurrence frequencies in the major peak region between 0.5 and 3 K. The operational and the recalculated BTDs behave differently at the right tail. For the recalculated BTDs, the occurrence frequencies of $(T_{10.8} - T_{12.0}) > 4$ K are strongly overestimated as a result of a revised and more consistent representation of the radiative impact of COSMO-DE ice-microphysics.

A similar comparison is performed for the normalized occurrence frequencies of $T_{8.7} - T_{10.8}$ in Fig 9. The observation shows a distribution function with a double peak: the primary peak is close to -3 K, and the secondary one occurs at around 0.5 K. The secondary peak is overestimated for the operational simulations. The position of the steep left distribution tail is shifted towards greater BTDs in all simulations which might be connected to a misrepresentation of the model boundary layer or land surface emissivity differences. The occurrence frequencies at the right tail are strongly overestimated in the two simulations, a deficit that becomes much clearer for the recalculated BTDs. Furthermore, the overall representation of the BTDs distribution is worse for the years 2013 and 2014 compared to 2012 as a result of changes in the cloud cover parameterization (not shown).

Finally, Fig. 9 contains an additional sensitivity setup based on variations of the crystal habit. As outlined in Appendix B, we implemented an approximate category mixing in which a generalized effective diameter of the mixture is calculated based on the cross-channel averaged apparent extinction behavior. The strategy was intentionally developed to improve representation of different frozen hydrometeor categories within the one-category interface of older RTTOV versions ($<$ v11). It is, however, useful to test the radiative effect of different hydrometeor shapes, which is termed habit variation in the following. Two different shapes have been tested. First, an approximate $D_{ge,mix}$ has been calculated for hexagonal ice crystals based on eq. (B.4) and used together with the RTTOV radiative properties of hexagonal shapes. Second, $D_{ge,mix}$ has been calculated based on snow aggregates and then used together with the RTTOV radiative properties of random aggregates. As expected and seen in Fig. 9, the two simulations based on different shapes show very similar occurrence frequencies for 10.8 μm. The window-channel BTDs are, however, very sensitive to the assumed shape and especially the right tails of the two BTD distributions as well as the secondary peak for the $(T_{8.7} - T_{10.8})$-frequencies are extremely sensitive to changes in the crystal habit. For the investigated channel differences, the sensitivity to crystal habit is much larger than the sensitivity to crystal size perturbations. This situation suggests that the representation of large BTDs (right tail) can be improved if COSMO-DE ice is partially converted to precipitating snow.

To shed more light on the origin of the functional form of the histograms, the respective contribution of several FWP categories to the total occurrence frequencies are shown with the help of stacked histograms in Fig. 10. Three different simulation setups are compared. The first is our reference setup in which COSMO-DE ice is considered as hexagonally shaped and COSMO-DE snow as aggregates, and the mixing and combination of radiative properties is applied in advance of RTTOV radiative transfer. The second and third consist of approximate mixtures which are either pure hexagonal or pure aggregates. For simulated $(T_{10.8} - T_{12.0})$-frequencies, the ice-free part (FWP = 0) has a broad maximum centered around 2 K (see Fig. 10). The positive BTDs mainly result from the different sensitivities of the two channels to lower tropospheric humidity. The 12.0 μm channel is slightly more affected by water vapor absorption, leading to an increased effective emission altitude, and thus colder emission temperatures compared to the 10.8 μm channel (Schmetz et al., 2002). For $T_{8.7} - T_{10.8}$, the part with FWP = 0 is much narrower and centered around -2.5 K, which is also caused by greater atmospheric emission altitudes of the 8.7 μm channel. The ice-affected occurrence frequencies are very similar between our reference setup and the pure hexagonal setup. This illustrates that hexagonal ice is dominating the radiative footprint of our reference. Semi-transparent ice strongly contributes to the tails of the simulated distributions, whereas semi-transparent snow behaves more comparable to the part with FWP = 0. For $(T_{10.8} - T_{12.0})$, thick ice mainly contributes to the left tail populating a broad range between 0 and 2 K. Thick snow aggregates lead to a very unrealistic peak around $(T_{10.8} - T_{12.0}) \approx 0$ K. For $T_{8.7} - T_{10.8}$, the location and magnitude of the secondary peak is mainly determined by contributions from larger FWP, thus thicker cirrus clouds. This therefore illustrates that even if the microphysical information in Meteosat SEVIRI images is limited, a careful evaluation of consistently derived BTD can help to point to deficits in the microphysical representation of a numerical model.

6. Conclusions

Uncertainties in ice-affected synthetic brightness temperatures are the focus of our investigation. In general, satellite images observed by imaging radiometers do have important applications in data assimilation and model evaluation. They have been used to characterize the representation of simulated cloudiness and the diurnal change in cloud radiative properties.

As cloud microphysical parameterizations in regional numerical models become increasingly more complex, a consistent treatment of microphysical hydrometeor properties within model-internal parts and in the satellite forward operators gains importance.

We therefore study the impact of systematic changes in frozen hydrometeor radiative properties towards increased consistency on the simulation of synthetic brightness temperatures of the imaging radiometer SEVIRI aboard Meteosat satellites. Numerical forecasts from the German regional weather model COSMO-DE have been selected for 74 summer convection days. Synthetic satellite images have been simulated using the fast radiative transfer model RTTOV and a revised scheme for the calculation of frozen-hydrometeor radiative properties. In a first step towards more consistency, subgrid-scale fractional cloud cover is adjusted, and the generalized effective diameters of the frozen hydrometeor categories ice, snow and graupel are calculated based on model microphysics. Second, the radiative cloud properties are derived for the frozen condensate categories separately, assuming hexagonal shapes for ice, random aggregates for snow and spherical shape for graupel. The category mixing is applied to the different cloud radiative properties, and the resulting mixture is input to RTTOV. This procedure enables a much closer match to the model-internal microphysical formulation than previously applied empirical relations with important implications for model evaluation.

Based on a comparison between operational synthetic brightness temperatures and ones recalculated with our revised scheme, we show that systematic changes in subgrid-scale cloud cover and crystal size induce changes up to 10 K for ice-affected window channel brightness temperatures. The BT changes are most pronounced for semi-transparent cirrus clouds. Furthermore to represent uncertainties in the cloud parameterizations, we study the sensitivity of infrared brightness temperatures to meaningful perturbations in cloud cover and crystal size. Therefore, relative perturbation of 20% in the subgrid-scale portion of cloud-free parts and 20% relative perturbation in crystal size are considered based on empirical relations presented by Quaas (2012) and McFarquhar et al. (2003), respectively. The maximum sensitivity appears for semi-transparent clouds having window-channel brightness temperatures around 240 and 260 K and integrated total frozen water paths around 30 gm^{-2}. Perturbations in cloud cover and crystal size lead to maximum changes between 4 and 5 K in infrared window-channel brightness temperatures. Absorbing infrared channels are less affected by prescribed perturbations due to stronger atmospheric contributions.

Furthermore, we discuss the problematic aspect of inconsistencies between model-internal and external formulations of cloud microphysical and radiative properties. We illustrate the impact of changes in ice-microphysics on the known cold bias of COSMO-DE, for which an $\approx 170\%$ overestimation of the occurrence of cold window channel brightness temperatures between 220 and 240 K is found. We show that the magnitude of the observed bias is sensitive to systematic changes in subgrid-scale cloud cover parameterization and particle size and habit. Thus, a significant portion of between 35% and 70% of the COSMO-DE cold bias can be attributed to the representation of ice clouds in the satellite forward operator. We additionally discuss the use of window-channel brightness temperature differences of the 8.7, 10.8 and 12.0 μm channels for the evaluation the model-internal microphysical formulation. Using a revised description of the satellite forward operator that is in fact now much more consistent with the model, we hypothesize that the occurrence frequencies of COSMO-DE ice are overestimated in convective situations. We also infer that the assumed shape or habit can have a strong influence on the realistic representation of brightness temperature differences.

The resulting sensitivity of synthetic observation to the details of the microphysics makes it clear that a consistent, explicit and well documented treatment of frozen hydrometeors is required. Further effort is needed to understand corresponding shortcomings and to reduce the bias between real and synthetic observations. We strongly emphasize that future reformulations of model-internal parameterizations take the route towards increasing consistency. One advanced and promising candidate is e.g. the microphysical formulation based on habit mixtures proposed by Baran et al. (2014a,b). We further recommend to consider consistency between model-internal microphysical formulations and observation-based retrieval algorithms that are used to infer cloud properties from the observations and to evaluate the model based on physical quantities.

In the next steps, we plan to apply the results of the current study to construct object-based metrics for forecast verification with geostationary satellite data. This is ongoing work which will help to assess the representation of cold clouds in COSMO-DE, their diurnal cycle as well as the inherent uncertainties in the verification process in more detail. We will further extend our activities toward the evaluation of the ICON model in large eddy simulation mode (see e.g. Heinze et al., 2016, for first results). This poses the new challenge of assessing the impact of cirrus radiative properties determined by a higher moment scheme resolving scales less than a kilometer.

Acknowledgements

The work has been partially funded within OASE project of the Hans Ertel Center for Weather Research coordinated by the German Weather Service and within the HD(CP)^2 S5 project funded by the BMBF under grant 01LK1507C. We thank two anonymous reviewers for their valuable comments on the manuscript. We acknowledge EUMETSAT for providing SEVIRI data, DWD for providing COSMO-DE forecasts and the EUMETSAT-NWPSAF team for providing RTTOV source code and support. Special thanks also to our DWD colleagues Annika Schomburg, Uli Blahak, Axel Seifert and Robin Faulwetter for comments on the manuscript and their help with the operational SynSat product. We further thank to Martin Rempel for case selection.

Appendix A. Calculation of generalized effective diameter from COSMO-DE microphysics

In general, the effective particle diameter is usually defined as ratio between the total particle volume V_{tot} and the total projected area A_{tot} (Foot, 1988; McFarquhar and Heymsfield, 1998; Wyser, 1998)

$$D_{eff} = \frac{3}{2}\frac{V_{tot}}{A_{tot}} = \frac{3}{2\,\rho_i}\,\frac{\mathrm{IWC}}{A_{tot}}\,. \tag{A.1}$$

The total particle volume can be approximately related to the volume-specific particle content, e.g. with $V_{tot} = \mathrm{IWC}/\rho_i$ using the bulk ice density of $\rho_i = 0.92 \times 10^3\ \mathrm{kg\,m^{-3}}$. For radiative calculations in RTTOV, however, the generalized effective diameter

$$D_{ge} = \frac{4\sqrt{3}}{9} D_{eff} \tag{A.2}$$

is used (Fu, 1996; McFarquhar et al., 2003).

The following calculation of D_{ge} is based on three assumptions: (i) the properties of hydrometeors in each grid cell can be determined from a given number size distribution $\mathcal{N}$ as function of the maximum dimension D_{max} whose parameters are determined by prognostic model variables, e.g. ice mixing ratio, (ii) to simplify the calculation of moments of $\mathcal{N}$, the size range of D_{max} is extended to zero and infinity, and (iii) the particle mass m and projected area A in each size bin are approximated by a power law relation,

$$m(D_{max}) = a_m \, (D_{max})^{b_m} \; , \tag{A.3}$$

$$A(D_{max}) = a_A \, (D_{max})^{b_A} \; . \tag{A.4}$$

Please note that spherical homogeneous particles have $b_A = 2$ and $b_m = 3$. For irregularly-shaped ice and snow particles, however, these coefficient can significantly deviate. The coefficients of the area relation are not constrained by the COSMO-DE microphysics which gives us some freedom to select reasonable values from literature, but also introduces uncertainty. We choose values tabulated in Mitchell (1996): for ice $(a_{A.i}, b_{A,i}) = (0.12, 1.85)$ from the small hexagonal plates habit, and for snow $(a_{A.i}, b_{A,i}) = (0.069, 1.75)$ from the rimed dendrites habit. Compared to Mitchell (1996), we changed the units of D_{max} and A to SI units. The ice water content and total projected area are then given by

$$\mathrm{IWC} = \int_0^\infty dD_{max} \, m(D_{max}) \mathcal{N}(D_{max}) = a_m \mathcal{M}_{b_m} \; , \tag{A.5}$$

$$A_{tot} = \int_0^\infty dD_{max} \, A(D_{max}) \mathcal{N}(D_{max}) = a_A \mathcal{M}_{b_A} \tag{A.6}$$

with fractional moment of the number size distribution $\mathcal{N}$ equal to

$$\mathcal{M}_b = \int_0^\infty dD_{max}\,(D_{max})^b \mathcal{N}(D_{max})\,. \tag{A.7}$$

With eq. (A.1) and (A.2), it follows that

$$D_{ge} = \frac{2\sqrt{3}}{3}\frac{a_m}{\rho_i\,a_A}\frac{\mathcal{M}_{b_m}}{\mathcal{M}_{b_A}}\,. \tag{A.8}$$

COSMO-DE ice is assumed to consist of thin hexagonal plates. In addition, a monodisperse size distribution is assumed for which all the particle mass is concentrated at a infinitely small particle size bin centered at D_i, i.e.

$$\mathcal{N}_i(D_{max}) = N_{0,i}\;\delta\,(D_{max} - D_i) \tag{A.9}$$

where the number of ice particles per volume is parameterized by

$$N_{0,i} = 1.0\times 10^2 \exp\left[0.2\,(T_0 - T)\right]\;\mathrm{m}^{-3}\,, \tag{A.10}$$

which uses the melting point $T_0 = 273.15$ K. In the above relation, T is set to 236.15 and 273.15 K for colder and warmer temperatures, respectively. The corresponding moments are given by $\mathcal{M}_b = N_{0,i}(D_i)^b$. With the help of the mass relation $m = a_{m,i}D_i^{b_{m,i}}$ with $a_{m,i} = 130\;\mathrm{kg\,m^{-3}}$ and $b_{m,i} = 3$ (taken from the model documentation), the maximum dimension D_i is related to IWC via

$$D_i = \left(\frac{\mathrm{IWC}}{a_{m,i}\,N_{0,i}}\right)^{1/b_{m,i}}\,. \tag{A.11}$$

Via eq. (A.8), we introduce the generalized effective diameter of COSMO-DE ice

$$D_{ge,i} = \frac{2\sqrt{3}}{3}\frac{a_{m,i}}{\rho_i\,a_{A,i}}\,(D_i)^{b_{m,i}-b_{A,i}}\,. \tag{A.12}$$

Following Baldauf et al. (2011), snow is assumed to be exponentially distributed with the number size distribution

$$\mathcal{N}_s(D_{max}) = N_{0,s} e^{-\lambda D_{max}} , \tag{A.13}$$

with the slope parameter λ and the intercept $N_{0,s}$. The latter depends on T and SWC and is calculated with the method of moments by Field et al. (2005). The moments of the expontial distribution are given by

$$\mathcal{M}_b = \frac{N_{0,s}\,\Gamma(b+1)}{\lambda^{b+1}} . \tag{A.14}$$

In addition, the mass relation $m(D_{max}) = a_{m,s}(D_{max})^{b_{m,s}}$ with $(a_{m.g}, b_{m,g}) = (0.038, 2)$ is used to calculate the slope parameter from the snow water content SWC as (see Baldauf et al. (2011))

$$\lambda = \left(\frac{N_{0,s}\, a_{m,s}\, \Gamma(b_{m,s}+1)}{\mathrm{SWC}} \right)^{1/(b_{m,s}+1)} . \tag{A.15}$$

Hence, the generalized effective diameter of COSMO-DE snow becomes

$$D_{ge,s} = \frac{2\sqrt{3}}{3} \frac{a_{m,s}}{\rho_i\, a_{A,s}} \frac{\Gamma(b_{m,s}+1)}{\Gamma(b_{A,s}+1)} \lambda^{b_{A,s}-b_{m,s}} . \tag{A.16}$$

Thus, the model-based D_{ge} of ice and snow depends exponentially on temperature due to a prescribed particle number function, and has a power law dependence on the hydrometeor mass content.

Furthermore, COSMO-DE graupel is also assumed to be exponentially distributed and hence determined by similar relations as COSMO-DE snow. Following, Baldauf et al. (2011), the intercept is fixed to $N_{0,g} = 4 \times 10^6$ m^{-4} and the mass-size relation is governed by the coefficients $(a_{m.g}, b_{m,g}) = (169.6, 3.1)$ for D_{max} and m in SI units. Thus, replacing $N_{s,0}$, $a_{m,s}$, $b_{m,s}$, and SWC in eq. (A.15) with their respective graupel counterparts fully determines the graupel particle size distributions. The given mass-relation coefficients related to the lump graupel type R4b given in (Heymsfield and Kajikawa, 1987, their table 2). For this hydrometeor type, Mitchell (1996) gives coefficient for the area-size relation of $(a_{A.g}, b_{A,g}) = (0.5, 2)$ also in SI units. The COSMO-DE graupel generalized effective diameter $D_{ge,g}$ is given by eq. (A.16) when corresponding parameters are inserted.

Appendix B. Approximate category mixing

In the following, we consider a method for mixing frozen hydrometeor categories in advance of radiative transfer calculations in order to still stay with the old one-category interface of the well established RTTOV routines. Here, we ignore the effect of graupel. This is a solution of intermediate complexity between the operational SynSat scheme which simply adds ice, snow and graupel content and the more sophisticated approach described above which infers the radiative properties of ice and snow separately.

From $D_{ge,i}$ and $D_{ge,s}$, an approximate generalized, effective diameter of the mixture $D_{ge,mix}$ is derived which produces a similar apparent extinction, i.e. $\tilde{\beta}_{mix} = \tilde{\beta}_i + \tilde{\beta}_s$. Using the regression models introduced by Fu (1996) and the coefficients internally given within RTTOV, it can be shown that $\tilde{\beta}_i$/IWC and $\tilde{\beta}_s$/SWC (in m^2/kg) can be represented by a power law dependence on $D_{ge,i}$ and D_{ge_s} (in μm) , respectively,

$$\frac{\tilde{\beta}_i}{\mathrm{IWC}} = a_{\beta,i} \left(D_{ge,i}\right)^{b_{\beta,i}} , \tag{B.1}$$

$$\frac{\tilde{\beta}_s}{\mathrm{SWC}} = a_{\beta,s} \left(D_{ge,s}\right)^{b_{\beta,s}} , \tag{B.2}$$

in the range of 20 - 100 μm with acceptable accuracy. Even though, the coefficients in the above relations strongly depend on the considered wavelength, the median coefficients $(a_{\beta,i}, a_{\beta,s}) = (13, 6) \times 10^2$ and $(b_{\beta,i}, b_{\beta,s}) =$

$(-1.0, -0.9)$ can be found. Assuming that the radiative properties of the mixture are sufficiently described by the behavior of hexagonal ice crystals, i.e.

$$\frac{\tilde{\beta}_{mix}}{\mathrm{IWC} + \mathrm{SWC}} = a_{\beta,i} \left(D_{ge,mix}\right)^{b_{\beta,i}} \ , \tag{B.3}$$

the above coefficients can be utilized to approximate the generalized effective diameter of the mixture as

$$D_{ge,mix} = \left[f_i \ \left(D_{ge,i}\right)^{b_{\beta,i}} + (1 - f_i) \frac{a_{\beta,s}}{a_{\beta,i}} \left(D_{ge,s}\right)^{b_{\beta,s}} \right]^{1/b_{\beta,i}} \ , \tag{B.4}$$

where the fraction of ice $f_i = \mathrm{IWC}/(\mathrm{IWC} + \mathrm{SWC})$ was defined. $D_{ge,mix}$ gives the effective size of ice particles with the content of IWC + SWC which lead to similar apparent extinction of infrared radiation as the sum of ice with effective size $D_{ge,i}$ and content IWC and snow with effective size $D_{ge,s}$ and content SWC. Generally, the apparent extinction depends on the wavelength, thus, eq. (B.4) is of approximate nature and typical relative deviations of $D_{ge,mix}$ range from 4 to 12%.

Appendix C. Variation of radiative properties at fixed average particle mass

To study the sensitivity of synthetic infrared imagery, perturbations with respect to generalized effective diameters D_{ge} are applied for the calculation of radiative properties, e.g. β_{abs} for absorption coefficient. These perturbations, however, are performed under the constraint of constant average particle mass. This restriction is needed as D_{ge} is calculated based on mass content, e.g. IWC, and temperature. An inverted IWC-to-D_{ge} relation would couple perturbations of D_{ge} to variations in IWC which is not wanted in our context as IWC is fully constrained by model simulations, however

D_{ge} is uncertain due to a less constrained relation for the projected particle area and due to a simplified particle size distribution.

We consider the absorption cross section per particle

$$\langle \sigma_{abs} \rangle = \int_0^\infty dD_{max}\, A(D_{max})\, n(D_{max})\, Q_{abs}(D_{max}) = \langle Q_{abs} \rangle_A \, \langle A \rangle \tag{C.1}$$

where $n(D_{max})$ is the normalized particle size distribution, i.e. $\mathcal{N}$ divided by the total number of particles N_{tot} per volume, and Q_{abs} and A are absorption efficiency and particle projected area, respectively. For the last step, the absorption efficiency was averaged over the particle size spectrum with the particle area as additional weight, and the average particle area $\langle A \rangle$ was introduced. The effective diameter (see eq. (A.1)) can be also stated in terms of average properties per particle, i.e.

$$D_{eff} = \frac{3}{2\,\rho_i} \, \frac{\langle m \rangle}{\langle A \rangle} \tag{C.2}$$

with the average mass per particle $\langle m \rangle$. Hence, absorption cross section per particle obeys

$$\langle \sigma_{abs} \rangle = \frac{3\,\langle Q_{abs} \rangle_A}{2\,\rho_i} \, \frac{\langle m \rangle}{D_{eff}} \tag{C.3}$$

Variations of $\langle \sigma_{abs} \rangle$ with respect to D_{eff} at constant $\langle m \rangle$ apply to $\langle Q_{abs} \rangle_A$ which is an implicit function of D_{eff} and the D_{eff}^{-1}-term in the formula above.

References

Baldauf, M., Seifert, A., Förstner, J., Majewski, D., Raschendorfer, M., Reinhardt, T., 2011. Operational Convective-Scale Numerical Weather Prediction with the COSMO Model: Description and Sensitivities. Mon. Wea. Rev. 139, 3887–3905.

Baran, A.J., 2012. From the single-scattering properties of ice crystals to climate prediction: A way forward . Atmos. Res. 112, 45 – 69.

Baran, A.J., Cotton, R., Furtado, K., Havemann, S., Labonnote, L.C., Marenco, F., Smith, A., Thelen, J.C., 2014a. A self-consistent scattering model for cirrus. II: The high and low frequencies. Quart. J. Roy. Meteor. Soc. 140, 1039–1057.

Baran, A.J., Hill, P., Furtado, K., Field, P., Manners, J., 2014b. A Coupled Cloud Physics-Radiation Parameterization of the Bulk Optical Properties of Cirrus and Its Impact on the Met Office Unified Model Global Atmosphere 5.0 Configuration. J. Climate 27, 7725–7752.

Bauer, P., Ohring, G., Kummerow, C., Auligne, T., 2011. Assimilating Satellite Observations of Clouds and Precipitation into NWP Models. Bull. Amer. Meteor. Soc. 92, ES25 – ES28.

Bauer, P., Thorpe, A., Brunet, G., 2015. The quiet revolution of numerical weather prediction. Nature 525, 47–55.

Baum, B.A., Yang, P., Heymsfield, A.J., Schmitt, C.G., Xie, Y., Bansemer, A., Hu, Y.X., Zhang, Z., 2011. Improvements in Shortwave Bulk Scattering and Absorption Models for the Remote Sensing of Ice Clouds. J. Appl. Meteor. Climatol. 50, 1037–1056.

Bikos, D., Lindsey, D.T., Otkin, J., Sieglaff, J., Grasso, L., Siewert, C., Correia Jr, J., Coniglio, M., Rabin, R., Kain, J.S., et al., 2012. Synthetic Satellite Imagery for Real-Time High-Resolution Model Evaluation. Wea. Forecasting 27, 784–795.

Bley, S., Deneke, H., Senf, F., 2016. Meteosat-based characterization of the spatiotemporal evolution of warm convective cloud fields over central europe. J. Appl. Meteor. Climatol. accepted.

Böhme, T., Stapelberg, S., Akkermans, T., Crewell, S., Fischer, J., Reinhardt, T., Seifert, A., Selbach, C., van Lipzig, N., 2011. Long-term evaluation of COSMO forecasting using combined observational data of the GOP period. Meteor. Z. 20, 119–132.

Chaboureau, J.P., Cammas, J.P., Mascart, P., Pinty, J.P., Claud, C., Roca, R., Morcrette, J.J., 2000. Evaluation of a cloud system life-cycle simulated by the Meso-NH model during FASTEX using METEOSAT radiances and TOVS-3I cloud retrievals. Quart. J. Roy. Meteor. Soc. 126, 1735–1750.

Chesters, D., Uccellini, L.W., Robinson, W.D., 1983. Low-Level Water Vapor Fields from the VISSR Atmospheric Sounder (VAS) Split Window Channels. J. Climate Appl. Meteor. 22, 725743.

Chevallier, F., Kelly, G., 2002. Model Clouds as Seen from Space: Comparison with Geostationary Imagery in the 11-μm Window Channel. Mon. Wea. Rev. 130, 712–722.

Chou, M.D., Lee, K.T., Tsay, S.C., Fu, Q., 1999. Parameterization for cloud longwave scattering for use in atmospheric models. J. Climate 12, 159–169.

Cintineo, R., Otkin, J.A., Xue, M., Kong, F., 2014. Evaluating the Performance of Planetary Boundary Layer and Cloud Microphysical Parameterization Schemes in Convection-Permitting Ensemble Forecasts Using Synthetic GOES-13 Satellite Observations. Mon. Wea. Rev. 142, 163–182.

van Diedenhoven, B., Ackerman, A.S., Cairns, B., Fridlind, A.M., 2014. A Flexible Parameterization for Shortwave Optical Properties of Ice Crystals. J. Atmos. Sci. 71, 1763–1782.

Eikenberg, S., Köhler, C., Seifert, A., Crewell, S., 2015. How microphysical choices affect simulated infrared brightness temperatures. Atmos. Res. 156, 67–79.

Field, P.R., Hogan, R.J., Brown, P.R.A., Illingworth, A.J., Choularton, T.W., Cotton, R.J., 2005. Parametrization of ice-particle size distributions for mid-latitude stratiform cloud. Quart. J. Roy. Meteor. Soc. 131, 1997–2017.

Foot, J.S., 1988. Some observations of the optical properties of clouds. II: Cirrus. Quart. J. Roy. Meteor. Soc. 114, 145–164.

Fu, Q., 1996. An Accurate Parameterization of the Solar Radiative Properties of Cirrus Clouds for Climate Models. J. Climate 9, 2058–2082.

Goody, R.M., Yung, Y.L., 1989. Atmospheric radiation : theoretical basis. Oxford University Press.

Görsdorf, U., Seifert, A., Lehmann, V., Köhler, M., 2011. Cloud statistics and NWP-model validation based on long-term measurements of a 35 GHz radar, in: Proccedings of 35th Conference on Radar Meteorology, Pittsburgh, PA, USA.

Heinze, R., Dipankar, A., Carbajal Henken, C., Moseley, C., Sourdeval, O., Trömel, S., Xie, X., Adamidis, P., Ament, F., Baars, H., Barthlott, C., Behrendt, A., Blahak, U., Bley, S., Brdar, S., Brueck, M., Crewell, S., Deneke, H., Di Girolamo, P., Evaristo, R., Fischer, J., Frank, C., Friederichs, P., Göcke, T., Gorges, K., Hande, L., Hanke, M., Hansen, A., Hege, H.C., Hoose, C., Jahns, T., Kalthoff, N., Klocke, D., Kneifel, S., Knippertz, P., Kuhn, A., Laar, T., Macke, A., Maurer, V., Mayer, B., Meyer, C.I., Muppa, S.K., Neggers, R.A.J., Orlandi, E., Pantillon, F., Pospichal, B., Röber, N., Scheck, L., Seifert, A., Seifert, P., Senf, F., Siligam, P., Simmer, C., Steinke, S., Stevens, B., Wapler, K., Weniger, M., Wulfmeyer, V., Zängl, G., Zhang, D., Quaas, J., 2016. Large-eddy simulations over Germany using ICON: A comprehensive evaluation. Quart. J. Roy. Meteor. Soc. submitted.

Heymsfield, A.J., Kajikawa, M., 1987. An improved approach to calculating terminal velocities of plate-like crystals and graupel. J. Atmos. Sci. 44, 10881099.

Illingworth, A.J., Barker, H.W., Beljaars, A., Ceccaldi, M., Chepfer, H., Clerbaux, N., Cole, J., Delano, J., Domenech, C., Donovan, D.P., et al., 2015. The EarthCARE Satellite: The Next Step Forward in Global Measurements of Clouds, Aerosols, Precipitation, and Radiation. Bull. Amer. Meteor. Soc. 96, 13111332.

Keil, C., Tafferner, A., Reinhardt, T., 2006. Synthetic satellite imagery in the Lokal-Modell. Atmos. Res. 82, 19–25.

Klinger, C., Mayer, B., 2016. The Neighboring Column Approximation (NCA) A fast approach for the calculation of 3D thermal heating rates in cloud resolving models. J. Quant. Spectrosc. Radiat. Transfer 168, 1728.

Köhler, C.G., Seifert, A., 2015. Identifying sensitivities for cirrus modelling using a two-moment two-mode bulk microphysics scheme. Tellus B 67.

Kostka, P.M., Weissmann, M., Buras, R., Mayer, B., Stiller, O., 2014. Observation Operator for Visible and Near-Infrared Satellite Reflectances. J. Atmos. Oceanic Technol. 31, 1216–1233.

Matricardi, M., Chevallier, F., Kelly, G., Thépaut, J.N., 2004. An improved general fast radiative transfer model for the assimilation of radiance observations. Quart. J. Roy. Meteor. Soc. 130, 153–173.

McFarquhar, G.M., Heymsfield, A.J., 1998. The Definition and Significance of an Effective Radius for Ice Clouds. J. Atmos. Sci. 55, 2039–2052.

McFarquhar, G.M., Iacobellis, S., Somerville, R.C.J., 2003. SCm simulations of tropical ice clouds using observationally based parameterizations of microphysics. J. Climate 16, 1643–1664.

Mitchell, D.L., 1996. Use of mass- and area-dimensional power laws for determining precipitation particle terminal velocities. J. Atmos. Sci. 53, 1710–1723.

Morcrette, J.J., 1991. Evaluation of Model-generated Cloudiness: Satellite-observed and Model-generated Diurnal Variability of Brightness Temperature. Mon. Wea. Rev. 119, 1205–1224.

Morrison, H., Milbrandt, J.A., 2015. Parameterization of Cloud Microphysics Based on the Prediction of Bulk Ice Particle Properties. Part I: Scheme Description and Idealized Tests. J. Atmos. Sci. 72, 287–311.

Okamoto, K., McNally, A.P., Bell, W., 2013. Progress towards the assimilation of all-sky infrared radiances: an evaluation of cloud effects. Quart. J. Roy. Meteor. Soc. 140, 1603–1614.

Otkin, J.A., Greenwald, T.J., 2008. Comparison of WRF Model-Simulated and MODIS-Derived Cloud Data. Mon. Wea. Rev. 136, 1957–1970.

Otkin, J.A., Greenwald, T.J., Sieglaff, J., Huang, H.L., 2009. Validation of a Large-Scale Simulated Brightness Temperature Dataset Using SEVIRI Satellite Observations. J. Appl. Meteor. Climatol. 48, 1613–1626.

Pavolonis, M.J., 2010. Advances in Extracting Cloud Composition Information from Spaceborne Infrared Radiances - A Robust Alternative to Brightness Temperatures. Part I: Theory. J. Appl. Meteor. Climatol. 49, 1992–2012.

Petty, G.W., 2006. A first course in atmospheric radiation. Sundog Pub.

Pfeifer, M., Yen, W., Baldauf, M., Craig, G., Crewell, S., Fischer, J., Hagen, M., Hünerbein, A., Mech, M., Reinhardt, T., Schröder, M., Seifert, A., 2010. Validating precipitation forecasts using remote sensor synergy: A case study approach. Meteor. Z. 19, 601–617.

Quaas, J., 2012. Evaluating the critical relative humidity as a measure of subgrid-scale variability of humidity in general circulation model cloud cover parameterizations using satellite data. J. Geophys. Res. 117.

Roca, R., Picon, L., Desbois, M., Le Treut, H., Morcrette, J.J., 1997. Direct comparison of meteosat water vapor channel data and general circulation model results. Geophys. Res. Lett. 24, 147–150.

Saunders, R., Matricardi, M., Brunel, P., 1999. An improved for assimilation of satellite radiance observations. Quart. J. Roy. Meteor. Soc. 125, 1407–1425.

Schmetz, J., Pili, P., Tjemkes, S., Just, D., Kerkmann, J., Rota, S., Ratier, A., 2002. An introduction to Meteosat Second Generation (MSG). Bull. Amer. Meteor. Soc. 83, 977–992.

Schomburg, A., Schraff, C., Potthast, R., 2014. A concept for the assimilation of satellite cloud information in an Ensemble Kalman Filter: single-observation experiments. Quart. J. Roy. Meteor. Soc. 141, 893–908.

Setvak, M., Lindsey, D.T., Novk, P., Wang, P.K., Radov, M., Kerkmann, J., Grasso, L., Su, S.H., Rabin, R.M., Stastka, J., et al., 2010. Satellite-observed cold-ring-shaped features atop deep convective clouds. Atmos. Res. 97, 80–96.

Slingo, A., Hodges, K.I., Robinson, G.J., 2004. Simulation of the diurnal cycle in a climate model and its evaluation using data from Meteosat 7. Quart. J. Roy. Meteor. Soc. 130, 1449–1467.

Sommeria, G., Deardorff, J.W., 1977. Subgrid-Scale Condensation in Models of Nonprecipitating Clouds. J. Atmos. Sci. 34, 344–355.

Stengel, M., Lindskog, M., Unden, P., Gustafsson, N., 2013. The impact of cloud-affected IR radiances on forecast accuracy of a limited-area NWP model. Quart. J. Roy. Meteor. Soc. 139, 2081–2096.

Strabala, K.I., Ackerman, S.A., Menzel, W.P., 1994. Cloud properties inferred from 8 - 12 μm data. J. Appl. Meteor. 33, 212–229.

Sundqvist, H., Berge, E., Kristjnsson, J.E., 1989. Condensation and Cloud Parameterization Studies with a Mesoscale Numerical Weather Prediction Model. Mon. Wea. Rev. 117, 1641–1657.

Thompson, G., Tewari, M., Ikeda, K., Tessendorf, S., Weeks, C., Otkin, J., Kong, F., 2016. Explicitly-coupled cloud physics and radiation parameterizations and subsequent evaluation in WRF high-resolution convective forecasts. Atmos. Res. 168, 92–104.

Vogel, R.L., Liu, Q., Han, Y., Weng, F., 2011. Evaluating a satellite-derived global infrared land surface emissivity data set for use in radiative transfer modeling. J. Geophys. Res. 116.

Waliser, D.E., Li, J.L.F., Woods, C.P., Austin, R.T., Bacmeister, J., Chern, J., Del Genio, A., Jiang, J.H., Kuang, Z., Meng, H., et al., 2009. Cloud ice: A climate model challenge with signs and expectations of progress. J. Geophys. Res. 114.

Wyser, K., 1998. The Effective Radius in Ice Clouds. J. Climate 11, 1793–1802.

Yang, P., Liou, K.N., Bi, L., Liu, C., Yi, B., Baum, B.A., 2015. On the radiative properties of ice clouds: Light scattering, remote sensing, and radiation parameterization. Adv. Atmos. Sci. 32, 32–63.

				8.7 – 10.8 μm			10.8 – 12.0 μm		
τ	D_{ge}/μm	IWC/(g m^{-3})	r_{depth}/km	Δr_{depth}/%	$\Delta\langle\sigma_{abs}\rangle$/%	$\Delta\langle\sigma_{sca}\rangle$/%	Δr_{depth}/%	$\Delta\langle\sigma_{abs}\rangle$/%	$\Delta\langle\sigma_{sca}\rangle$/%
0.01	20	2.5×10^{-4}	68.2	17.6	-21.6	130.6	17.7	-18.2	-45.5
0.10	30	2.6×10^{-3}	9.6	11.0	-14.9	79.4	12.1	-10.3	-30.8
0.72	50	3.0×10^{-2}	1.4	4.9	-7.7	34.7	5.5	-1.9	-17.9
3.05	80	0.21	0.3	0.9	-2.0	9.9	-0.1	4.1	-10.4
5.69	100	0.49	0.2	-0.2	-0.4	7.0	-1.5	5.3	-9.1

Table 1: Typical values of infrared penetration depth r_{depth} at 10.8 μm wavelength for homogeneous cirrus clouds. Generalized effective particle diameter D_{ge} and ice water content IWC are linked by conversion relations given by McFarquhar et al. (2003). τ is the infrared cloud-optical depth in nadir view for a one-kilometer thick cirrus cloud. Δr, $\Delta\langle\sigma_{abs}\rangle$ and $\Delta\langle\sigma_{sca}\rangle$ give the difference in penetration depth, absorption cross section and scattering cross section per particle for the channel combinations 8.7 and 10.8 μm as well as 10.8 and 12.0 μm relative to the value at 10.8 μm wavelength in percent. Numbers are based on RTTOV internal radiative property calculations for hexagonal crystal shape.

List of Figure Captions

Figure 1: Example scene at 5 July 2012 at 12 UTC / 13 LT. Compared are (a) operationally provided BT of the 10.8 μm channel in K, and (b) ice, (c) snow and (d) graupel water path from COSMO-DE in gm^{-2} and logarithmic color scaling as well as (e) SEVIRI BT10.8 and (f) FWP for Meteosat-8 observations. For BT10.8, color-enhancement is used (Setvak et al., 2010), in which values greater than 240 K are shown in gray shades with darker colors for warmer BTs, and values between 240 and 210 K in rainbow colors. Meteosat FWP is derived by the KNMI cloud physical properties algorithm further described in Bley et al. (2016).

Figure 2: Functional relationship for the IWC-to-D_{ge} conversion based on fits given in McFarquhar et al. (2003). The base-case (thick solid line), $\pm\sigma$ (inner dashed lines, shaded interval) and $\pm 2\sigma$ cases (outer dashed lines) are given. For illustration, a Gaussian distribution with equal mean and standard deviation as the calculated generalized effective diameter D_{ge} at 0.5 gm^{-3} is indicated at the y axis.

Figure 3: Occurrence frequencies of generalized effective diameter of (a) ice $D_{ge,i}$, (b) snow $D_{ge,s}$, and (c) graupel $D_{ge,g}$ in relation to the D_{ge} calculated from the McFarquhar et al. (2003) base case. Shown are occurrence frequencies constructed from all 296 COSMO-DE scenes and normalized by its respective maximum value with logarithmic color scale. The one-to-one line is shown for guidance. As graupel joint occurrence frequencies fall onto one line they have been plotted with filled circles for improved clearness with

colors indicating the normalized occurrence frequency. Dashed lines in panels (b) and (c) mark the range of the respective previous plot. The further panels show the occurrence frequencies of (d) particle sizes, (e) water path, and (f) relative fraction of the water path to the total frozen water path for ice (green solid line), snow (red), and graupel (blue). For (e) and (f), binning was performed in logarithmic scale and zero water path values have been included.

Figure 4: Color-enhanced BT10.8 (upper row) and BT10.8 difference (lower row) for the example scene already given in Fig. 1. We show the simulation results of independent revisions of (a, d) cloud cover, (b, e) generalized effective diameter, as well as (c, f) the fully revised scheme. The BT10.8 difference was calculated with respect to a reference simulation with operational SynSat settings. All values are given in K.

Figure 5: Occurrence frequency bias of BT10.8 relative to the operational setup (upper row) and to the Meteosat observation (lower row). Independent changes in the formulation of (a, d) cloud cover, (b, e) generalized effective diameter, and (c, f) the fully revised scheme are shown. Median values (thick black lines) and interquartile range (gray-shaded intervals) are calculated over all 296 COSMO-DE scenes. The frequency bias of the example scene of Fig. 1 is added as dashed blue lines. The case-to-case median frequency bias of the operational SynSat relative to the observation is added to each panel in the lower row with red solid lines for completeness.

Figure 6: Similar to Fig. 4d-f, but for the BT10.8 standard deviation for

perturbations in (a) subgrid-scale cloud cover and (b) crystal size.

Figure 7: Two-dimensional frequency plots for occurrence of BT deviations conditioned on occurrence of a reference BT of the revised scheme for 3 infrared MSG SEVIRI channels at 6.2, 7.3 and 10.8 μm (1st to 3rd row) and the BTDs $T_{10.8} - T_{12.0}$ (4th row) and $T_{8.7} - T_{10.8}$ (5th row), as well as two perturbation setups: cloud cover perturbation (left) and crystal size perturbation (right). Relative frequencies (color shades) have been normalized to one for each average BT bin. Median and upper / lower quartiles have been drawn by solid and dashed lines, respectively. Please note that the range of typical BTs differs for different channels (x-axis), increasing from (210, 240) K and (210, 260) K for the water vapor channels at 6.2 and 7.3 μm up to (210, 300) K for the window channel at 10.8 μm.

Figure 8: Same as Fig. 7, but conditioned on 10-based logarithm of total frozen water path.

Figure 9: Normalized median occurrence frequencies of $T_{10.8}$ (left), $T_{10.8} - T_{12.0}$ (middle), and $T_{8.7} - T_{10.8}$ (right) are shown for SEVIRI observation (1st row), operational DWD synthetic satellite data (2nd row), the recalculated BTs (3rd and 4th row). The interquartile range of scene-to-scene variability is given with shaded intervals, in all except the bottom row. The SEVIRI observations appear in every plot with dashed lines (median) and light gray shades. Maximum values of respective SEVIRI median occurrence frequencies have been taken for normalization. The black shaded intervals denote the range between the two median oc-

currence frequencies obtained by particle size perturbation (3rd row) and habit variation (4th row).

Figure 10: Normalized occurrence frequencies of (a-c) $T_{10.8} - T_{12.0}$, and (d-f) $T_{8.7} - T_{10.8}$ stacked for different total frozen water path (FWP) intervals: FWP $= 0$ gm^{-2} (black); (0, 10) gm^{-2} (dark gray); (10, 100) gm^{-2} (gray); and FWP > 100 gm^{-2} (light gray). The simulation were done for three different setups: the reference mixture with ice as hexagonally shaped and snow as aggregates (left), the approximate mixture based on pure hexagonal (middle) and based on pure aggregates (right). The maximum in the standard mixture has been used for normalization.

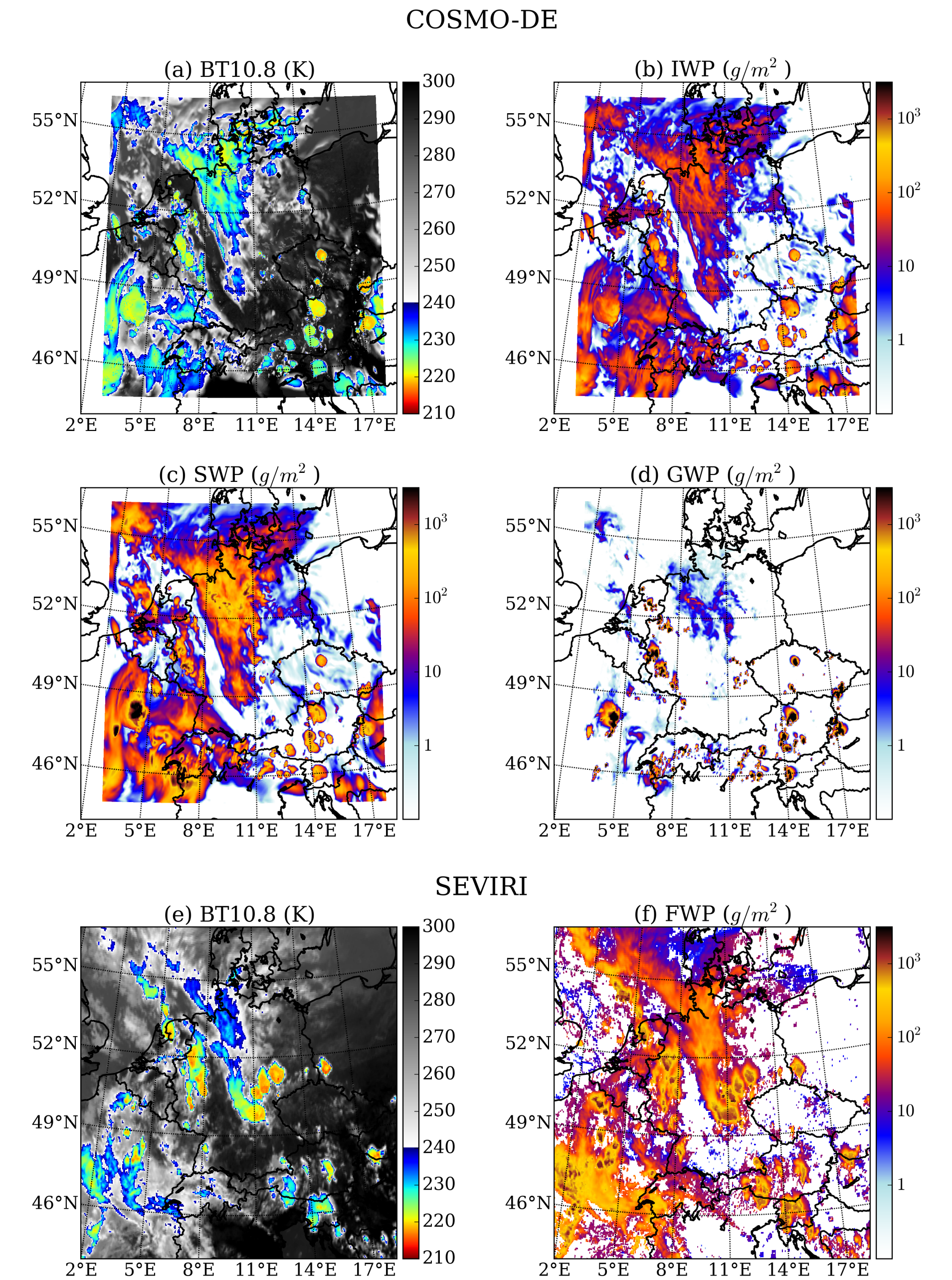

Figure 1: Example scene at 5 July 2012 at 12 UTC / 13 LT. Compared are (a) operationally provided BT of the 10.8 μm channel in K, and (b) ice, (c) snow and (d) graupel water path from COSMO-DE in gm^{-2} and logarithmic color scaling as well as (e) SEVIRI BT10.8 and (f) FWP for Meteosat-8 observations. For BT10.8, color-enhancement is used (Setvak et al., 2010), in which values greater than 240 K are shown in gray shades with darker colors for warmer BTs, and values between 240 and 210 K in rainbow colors. Meteosat FWP is derived by the KNMI cloud physical properties algorithm further described in Bley et al. (2016).

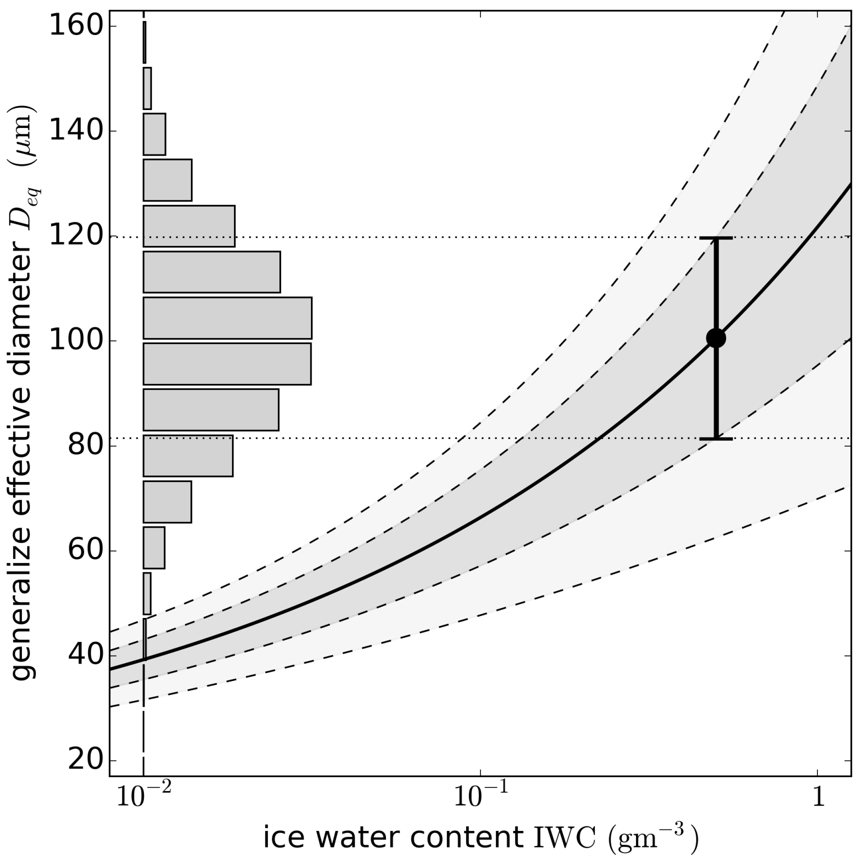

Figure 2: Functional relationship for the IWC-to-D_{ge} conversion based on fits given in McFarquhar et al. (2003). The base-case (thick solid line), $\pm\sigma$ (inner dashed lines, shaded interval) and $\pm 2\sigma$ cases (outer dashed lines) are given. For illustration, a Gaussian distribution with equal mean and standard deviation as the calculated generalized effective diameter D_{ge} at 0.5 $\mathrm{gm^{-3}}$ is indicated at the y axis.

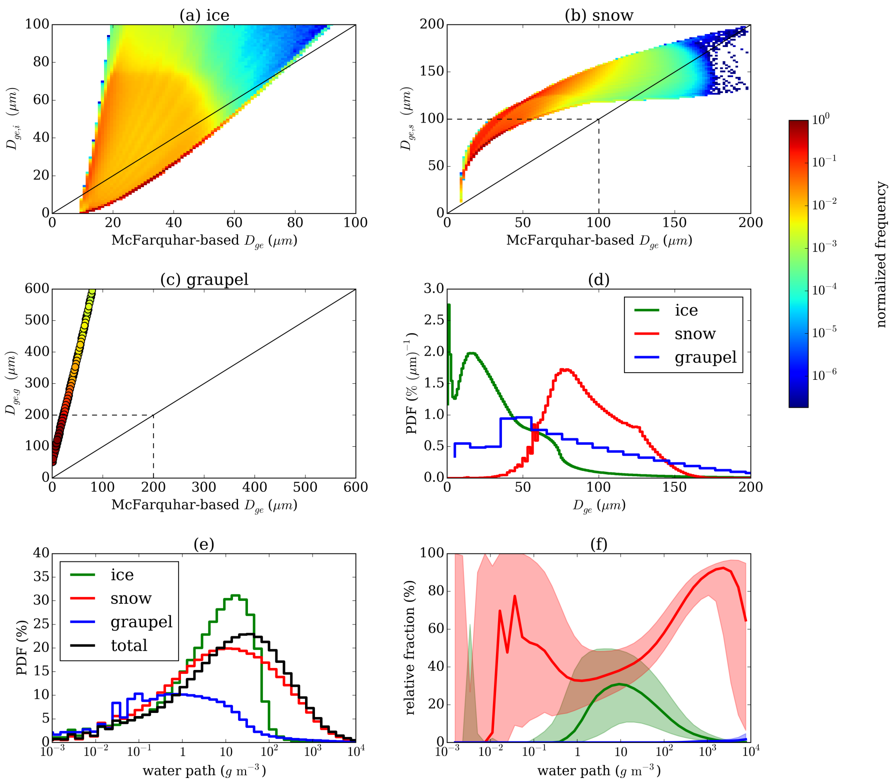

Figure 3: Occurrence frequencies of generalized effective diameter of (a) ice $D_{ge,i}$, (b) snow $D_{ge,s}$, and (c) graupel $D_{ge,g}$ in relation to the D_{ge} calculated from the McFarquhar et al. (2003) base case. Shown are occurrence frequencies constructed from all 296 COSMO-DE scenes and normalized by its respective maximum value with logarithmic color scale. The one-to-one line is shown for guidance. As graupel joint occurrence frequencies fall onto one line they have been plotted with filled circles for improved clearness with colors indicating the normalized occurrence frequency. Dashed lines in panels (b) and (c) mark the range of the respective previous plot. The further panels show the occurrence frequencies of (d) particle sizes, (e) water path, and (f) relative fraction of the water path to the total frozen water path for ice (green solid line), snow (red), and graupel (blue). For (e) and (f), binning was performed in logarithmic scale and zero water path values have been included.

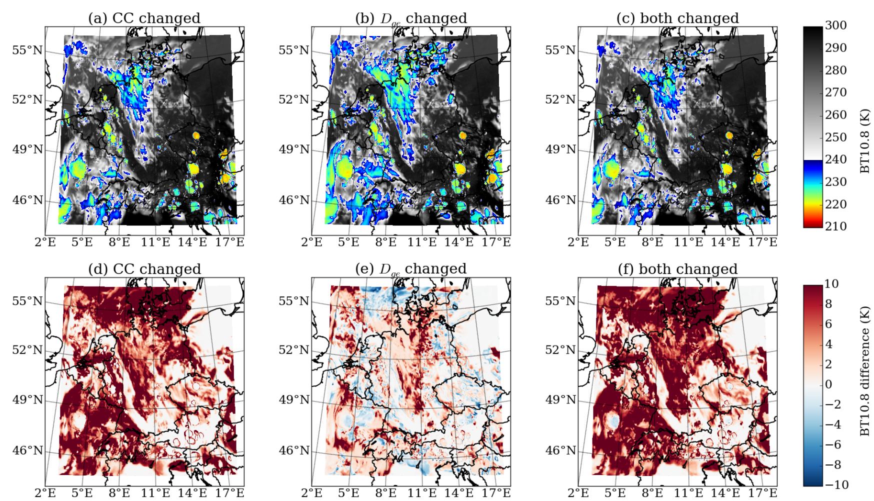

Figure 4: Color-enhanced BT10.8 (upper row) and BT10.8 difference (lower row) for the example scene already given in Fig. 1. We show the simulation results of independent revisions of (a, d) cloud cover, (b, e) generalized effective diameter, as well as (c, f) the fully revised scheme. The BT10.8 difference was calculated with respect to a reference simulation with operational SynSat settings. All values are given in K.

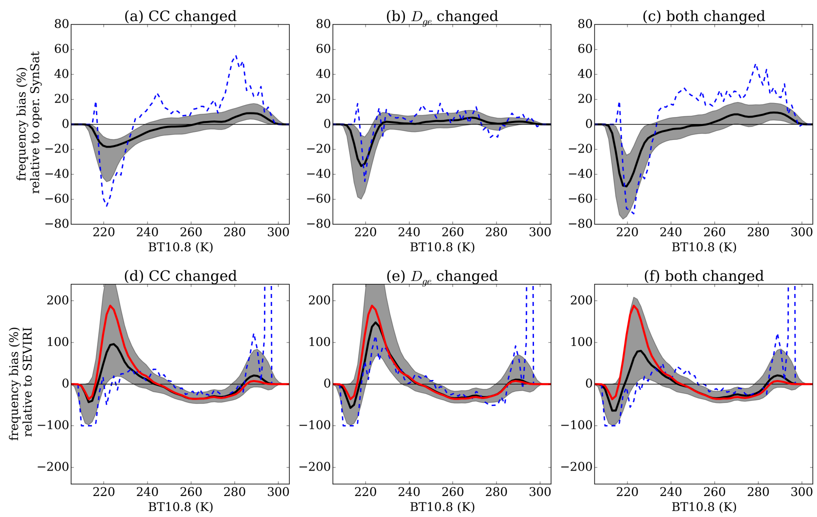

Figure 5: Occurrence frequency bias of BT10.8 relative to the operational setup (upper row) and to the Meteosat observation (lower row). Independent changes in the formulation of (a, d) cloud cover, (b, e) generalized effective diameter, and (c, f) the fully revised scheme are shown. Median values (thick black lines) and interquartile range (gray-shaded intervals) are calculated over all 296 COSMO-DE scenes. The frequency bias of the example scene of Fig. 1 is added as dashed blue lines. The case-to-case median frequency bias of the operational SynSat relative to the observation is added to each panel in the lower row with red solid lines for completeness.

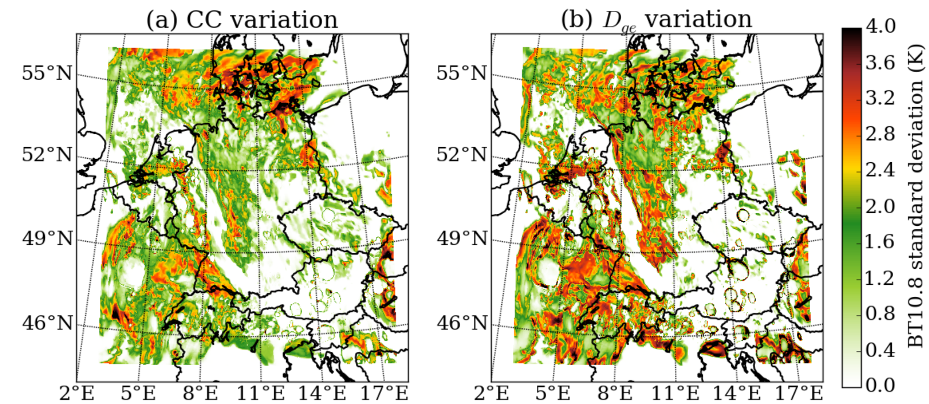

Figure 6: Similar to Fig. 4d-f, but for the BT10.8 standard deviation for perturbations in (a) subgrid-scale cloud cover and (b) crystal size.

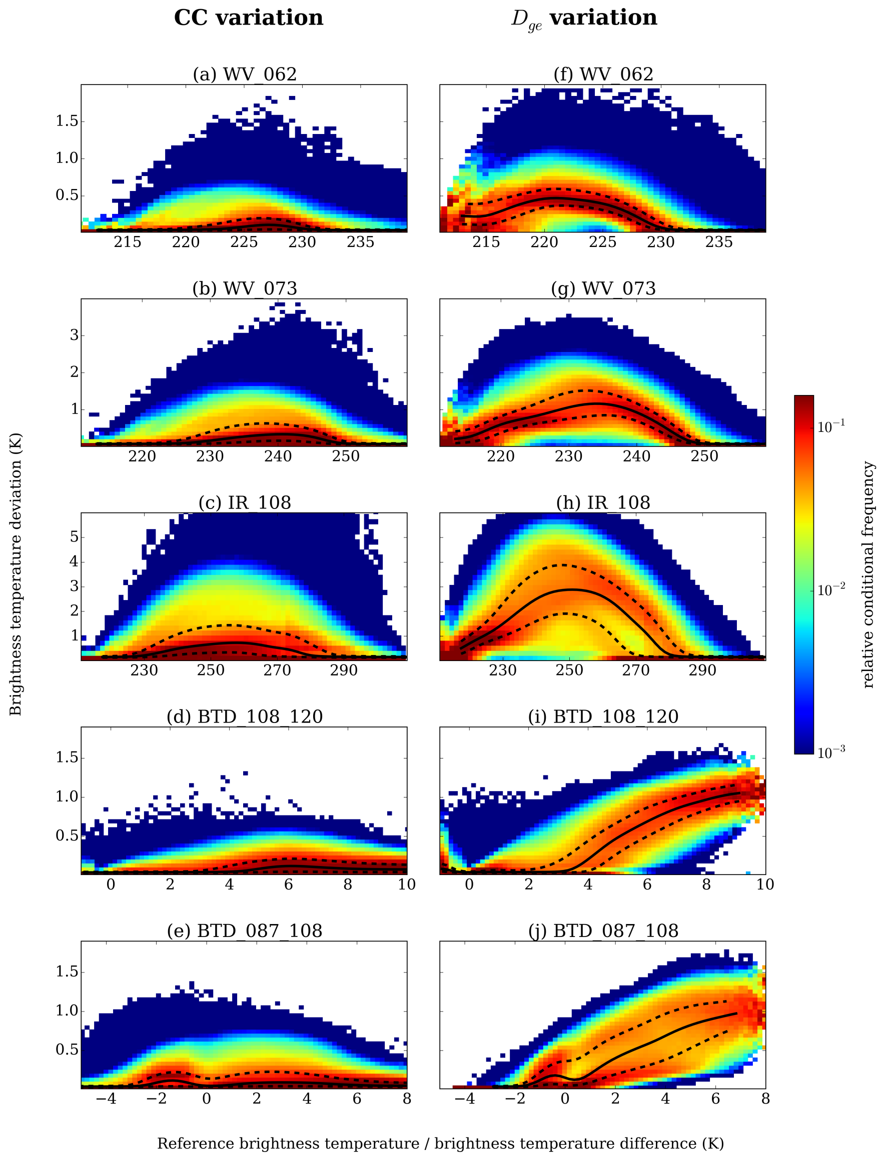

Figure 7: Two-dimensional frequency plots for occurrence of BT deviations conditioned on occurrence of a reference BT of the revised scheme for 3 infrared MSG SEVIRI channels at 6.2, 7.3 and 10.8 μm (1st to 3rd row) and the BTDs $T_{10.8} - T_{12.0}$ (4th row) and $T_{8.7} - T_{10.8}$ (5th row), as well as two perturbation setups: cloud cover perturbation (left) and crystal size perturbation (right). Relative frequencies (color shades) have been normalized to one for each average BT bin. Median and upper / lower quartiles have been drawn by solid and dashed lines, respectively. Please note that the range of typical BTs differs for different channels (x-axis), increasing from (210, 240) K and (210, 260) K for the water vapor channels at 6.2 and 7.3 μm up to (210, 300) K for the window channel at 10.8 μm.

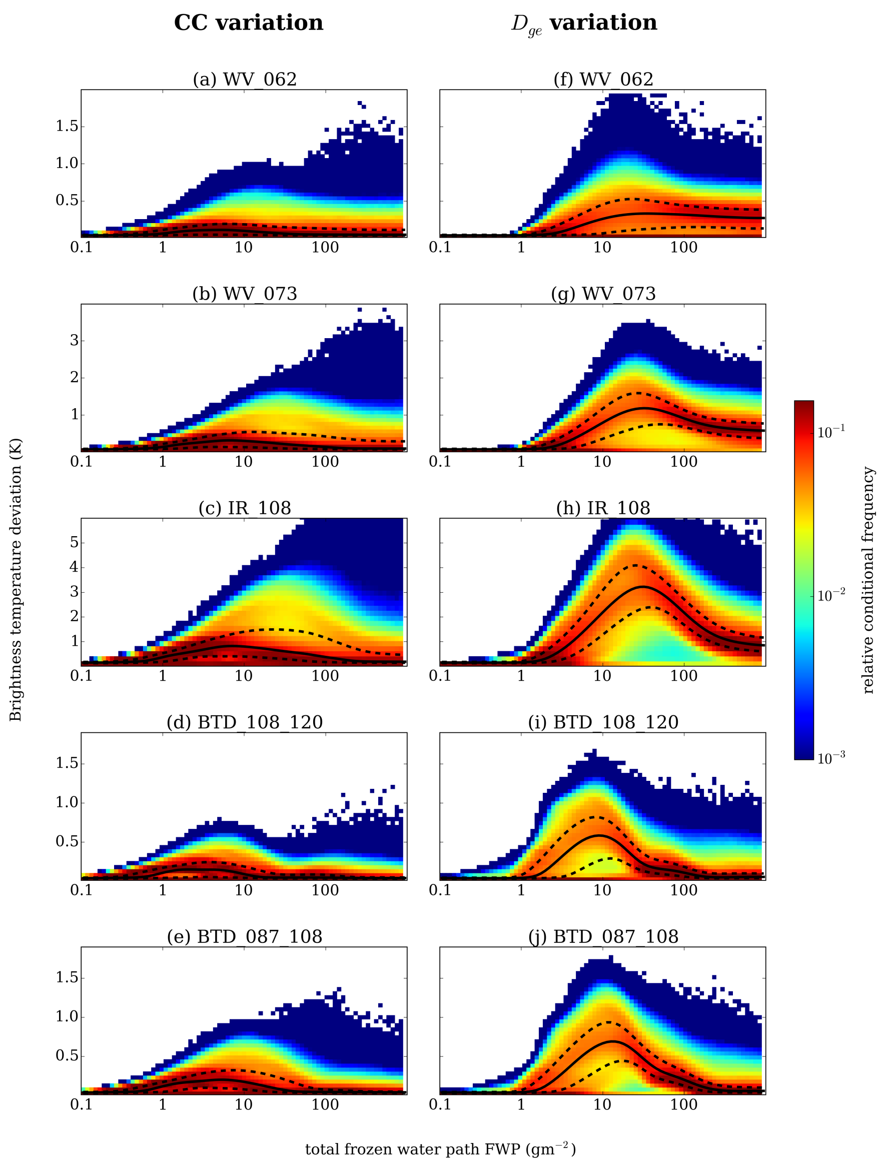

Figure 8: Same as Fig. 7, but conditioned on 10-based logarithm of total frozen water path.

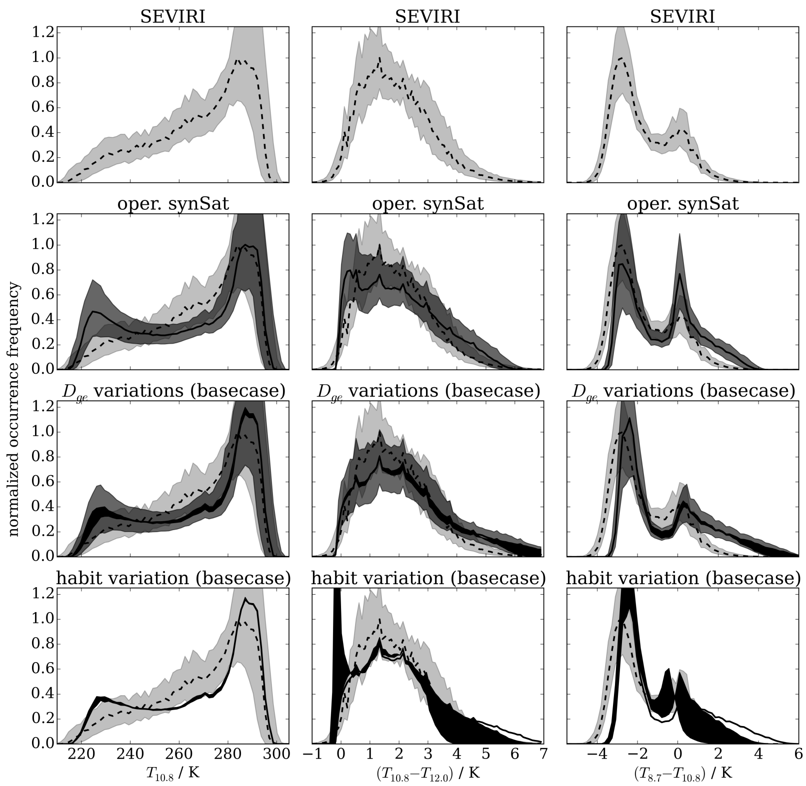

Figure 9: Normalized median occurrence frequencies of $T_{10.8}$ (left), $T_{10.8} - T_{12.0}$ (middle), and $T_{8.7} - T_{10.8}$ (right) are shown for SEVIRI observation (1st row), operational DWD synthetic satellite data (2nd row), the recalculated BTs (3rd and 4th row). The interquartile range of scene-to-scene variability is given with shaded intervals, in all except the bottom row. The SEVIRI observations appear in every plot with dashed lines (median) and light gray shades. Maximum values of respective SEVIRI median occurrence frequencies have been taken for normalization. The black shaded intervals denote the range between the two median occurrence frequencies obtained by particle size perturbation (3rd row) and habit variation (4th row).

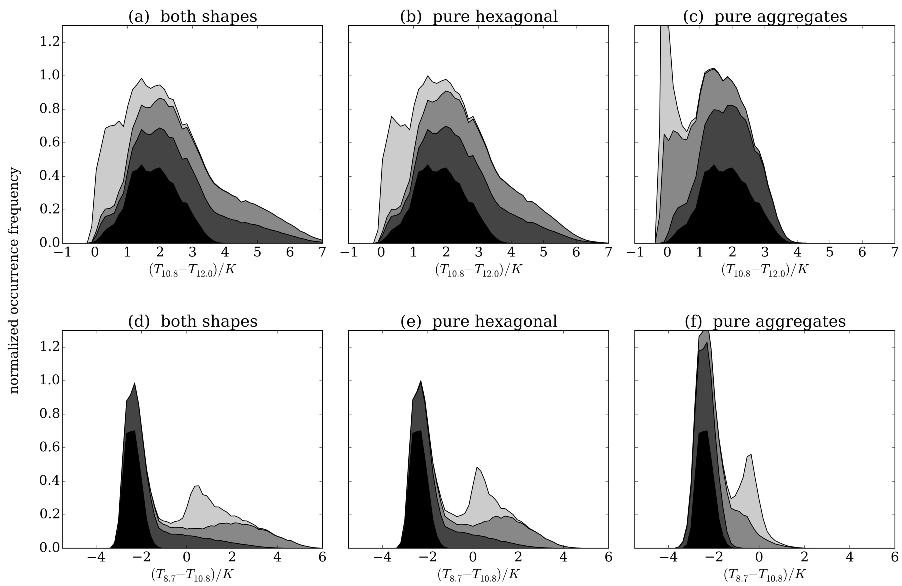

Figure 10: Normalized occurrence frequencies of (a-c) $T_{10.8} - T_{12.0}$, and (d-f) $T_{8.7} - T_{10.8}$ stacked for different total frozen water path (FWP) intervals: FWP = 0 gm^{-2} (black); (0, 10) gm^{-2} (dark gray); (10, 100) gm^{-2} (gray); and FWP > 100 gm^{-2} (light gray). The simulation were done for three different setups: the reference mixture with ice as hexagonally shaped and snow as aggregates (left), the approximate mixture based on pure hexagonal (middle) and based on pure aggregates (right). The maximum in the standard mixture has been used for normalization.